Ionospheric Disturbances generated by the 2015 Calbuco Eruption: Comparison of GITM-R simulations and GNSS observations

J. Tyska[1], Y. Deng[1], S. Zhang[2], and C. Y. Lin[3]

[1]University of Texas at Arlington.

[2]Massechusetts Institute of Technology Haystack Observatory

[3]National Central University, Taoyuan, Zhongli District, Taiwan

Corresponding author: Yue Deng (yuedeng@uta.edu)

Key Points:

- GNSS TEC data analysis for the first phase of the 2015 Calbuco eruption shows varied acoustic (A) and gravity (G) dominant perturbations.
- A simplified source representation and spectral A-G wave model are used to drive GITM-R to capture meso-scale perturbations near the source.
- The relative significance and phase speeds of acoustic and gravity wave driven ionospheric disturbance is reproduced in GITM-R simulations.

Abstract

Volcanic eruptions provide broad spectral forcing to the atmosphere and many previous studies have examined the IT disturbances caused by volcanic eruptions through both observations and modeling. Understanding the primary mechanisms that are relevant to explain the variety in waveform characteristics is still an important open question for the community. In this study, Global Navigation Satellite System (GNSS) Total Electron Content (TEC) data are analyzed and compared to simulations performed by the Global Ionosphere-Thermosphere Model with Local Mesh Refinement (GITM-R) for the first phase of the 2015 Calbuco eruption that occurred on 22 April. A simplified source representation and spectral acoustic-gravity wave (AGW) propagation model are used to specify the perturbation at the lower boundary of GITM-R at 100 km altitude. This modeling specification shows a good agreement with GNSS observations for some waveform characteristics such as travel/onset times and relative magnitudes. Most notably, GITM-R is able to reproduce the significance of AGWs as a function of radial distance from the vent, showing acoustic dominant forcing in the near field (<500 km) and gravity dominant forcing in the far-field (>500 km). The estimated apparent phase speeds from GITM-R simulations are consistent with observations with ~10% difference from observation for both acoustic wave packets and a trailing gravity mode. Relevance of the simplifications made in the lower atmosphere are then discussed and test changes to the assumed propagation structure, from direct propagation to ground-coupled propagation, show some improvement to the data-model comparison, especially the second acoustic wave-packet.

Plain Language Summary

The two eruption phases of the 2015 Calbuco volcanic event created atmospheric pressure and gravity disturbances that were measured as plasma disturbances in the earth's upper atmosphere by global navigation satellites. This study utilizes a fully self-consistent global circulation model of the upper atmosphere, with a highly flexible resolution, to simulate and investigate our understanding of the coupled atmosphere-plasma system in the event of a volcanic eruption. It is shown that the current methodology is capable of recreating important features of the observed upper atmospheric signals which include magnitude distributions, arrival times, and the relative contributions of pressure and gravity influenced waves as a function of distance from the volcano.

1 Introduction

It has been known for some time that explosive events can generate acoustic-gravity waves (AGWs) that then propagate, by virtue of the atmosphere's density profile, to thermospheric heights and influence the ionosphere in a way detectable by dual frequency Global Navigation Satellite Systems (Hines, 1960; klobuchar, 1985; Cheng, & Huang, 1992; Komjathy et al., 2012; Kouchk$\acute{a}$ et al., 2021). Kanimori & Harkrider (1994) demonstrated that point source forcing in an isothermal atmosphere, depicting injection of mass (or energy), resulted in two dominant modes, one less than the buoyant frequency (dependent on the vertical propagation angle, a gravity mode) and the other above the acoustic cut-off frequency. It had been shown previously from Liu & Yeh, (1971) and Chimonas & Hines, (1970) that the far field response of relatively localized sources is heavily influenced by the buoyant, gravity, and acoustic modes, suggesting that these frequencies may explain some of the dominant structures present in the Ionosphere-Thermosphere (IT) system as a direct consequence of a volcanic eruption.

The atmospheric and seismic signals created by volcanic eruptions have been examined extensively and many have documented the acoustic and gravity modes dominant in different data inquiries related to various eruptions (Mauk, 1982; Ripepe, et al., 2016; De Angelis et al., 2011; Kanamori & Watada, 1992; Yue et al., 2022; Shestakov, et al., 2021). Progresses in observational capabilities, primarily advances in GNSS infrastructure, have allowed for a variety of Covolcanic Ionospheric Disturbance(s) (CVIDs) to be detected and the subsequent analysis shows promise for using relative CVID magnitudes as indicators for various source parameters, such as energy estimation, ground peak velocity and plume height (Manta, et al., 2021; Dautermann et al, 2009;). The recent Tonga eruption has sparked additional interest in CVIDs due in particular to its global impact that initiated many interesting features. A few of the known

ionospheric impacts, that are of explanatory importance to the community, include the horizontally broad ionospheric hole that persisted ~10 hrs after the eruption (Aa et al. 2022), the variety of observed TID phase speeds that can be used to suggest the excitation of, and distinguish, various modes (Zhang et. al. 2022; Liu et. al., 2022; Pradipta et. al. 2023;), suppression and X-pattern merging of the equatorial ionization anomaly (Aa et. al., 2022; Zhang, K. et. al., 2022) as well as the formation of equatorial plasma bubbles (Aa et. al., 2022; Huba et. al., 2023), and the upper atmospheric manifestation of surface waves such as the lamb wave (cited in most above; Matoza et. al. 2022; Vadas et al. 2023). The unprecedented data coverage from a variety of instruments allows for an attempt at a cohesive understanding of energy redistribution in the coupled lithosphere-ocean-atmosphere-ionosphere-magnetosphere system, however such coverage should be supplemented with detailed modeling to infer causal links between observed CVIDs and known physical processes.

CVIDs observed following main eruption phases are typically categorized as one of two types in the measured total electron content (TEC) signals (Cahyadi et al., 2021). Thought to be indicative of the eruption dynamics, the first type (T1) consists of N-shaped pulses and are associated with acoustic/shock perturbations created by sudden, sufficiently intense explosions, like a vulcanian eruption (and similarly, manmade explosions (Kundu et. al. 2021)). The second type (T2) is thought to be associated with a continuous eruption style, such as Plinian or sub-Plinian eruptions, and comes in the form of Quasi-periodic TEC oscillations with dominant AGW modes (Cahyadi, et. al. 2020; Astafyeva, 2019). As a consequence of the source variability (size, intensity, duration, etc.) the TEC data associated with CVIDs show a variety of waveform characteristics. Typical magnitudes are often of the order ~0.1-0.9 TECU and have been shown to correlate with eruption intensity, either with respect to the Volcanic Explosivity Index (VEI)

or a more formal estimation of energy release (Cahyadi, et al., 2020; Heki, 2006; Dautermann et al., 2009). However, several authors have stressed the use of a relative measure for proper feature extraction, or comparisons, as magnitudes of TEC from GNSS observations are also heavily influenced by the local geomagnetic field orientation, background ionospheric conditions (such as ion/electron density climatography/weather), and line of site (LOS) satellite-receiver geometry (Cahyadi, et al., 2020; Inchin, 2020; Zettergren & Snively, 2015).

The spectral content of the ionospheric response is mostly acoustic dominant with spectral peaks typically cited around the acoustic-cutoff frequency of the neutral atmosphere (~3.6-3.8 mHz). The exact peak can be slightly higher or lower than the acoustic-cut off frequency components, indicating the coupling of additional dynamics (Lognone et al., 1998; Nakashima et al., 2016; Watada, & Kanamori , 2010). Although gravity wave modes are not always present in the TEC data during a volcanic eruption, several studies have documented disturbances with dominant peaks at 1-2 mHz (Yue, et al., 2022; Lindstrom, 2015). Additionally, theory and observational evidence from mesospheric airglow and satellite images indicate the generation of gravity waves (GWs) from volcanic eruptions should not be neglected (Miller, et al., 2015; Cappucci, 2021). Travel time diagrams of TEC data show that apparent phase speeds can range from ~1000-600 m/s for disturbances predominately in the acoustic range, and ~100-300 m/s predominately for lower frequency gravity wave modes (Heki et. al. 2006; Nakashima et al., 2015; Zhang et al., 2022; Liu et al., 2022; Yue et al., 2022). T1 disturbances often arrive in the IT system in ~8-12 minutes, roughly corresponding to propagation at the sound speed, due to their predominately acoustic nature, while T2 disturbances can take anywhere from ~14-60 minutes. The difference in travel times and TEC waveform characteristics between T1 and T2

disturbances does not appear to be solely influenced by the dominant spectral content and is perhaps a consequence of the AGW forcing mechanism for a particular eruption.

Although observational evidence for CVIDs is quite pronounced, attempts to simulate these events have been few and far between. Most methodologies use raytracing of a simplified forcing function (typically a gaussian-like, or a successive derivative) and consider ionospheric dynamics by utilizing the momentum/continuity equations for an assumed electron density distribution (Heki, 2006; Dautermann et al., 2008; Kundu et al., 2021; Heki & Fujimoto, 2022). These methodologies have shown good agreement with fitting N-shaped TEC variations to N-shaped forcing functions. Using a similar approach, Dautermann et al. (2008) showed the importance of AGW dispersion in explaining the observed acoustic wave trains and later considered the eigenmodes of a coupled earth-atmosphere model to drive the ionospheric disturbances (Dautermann et al., 2009). Their results showed that both strain meters in the earth and GPS-TEC signals could be explained by a single explosive atmospheric source and that the observed wave packets in the IT system are a consequence of the superposition of the three least attenuated modes. Zettergren & Snively (2015) were the first to use a two-dimensional (2D) compressible atmospheric model in conjunction with a multi-species 2D ionospheric model to investigate plasma responses to volcano like forcing, albeit under the guise of a generalized forcing function for natural hazards. Nevertheless, the dominant predicted acoustic periods match well to that of analyzed CVID events and their simulations showed quantitatively how the source characteristics and local geomagnetic field orientation influence the ionospheric response.

While lots of progresses have been made to understand the IT disturbance caused by geographic events through both observations and modeling, understanding the primary mechanisms that are relevant to explain the variety of waveform characteristics found in the

system is still an important open question for the community. The current literature on simulated CVIDs is lacking in two key areas. First, the raytracing methodologies all assume some simplified form of the complex coupling occurring in the IT system and this comes at the price of self-consistency when compared to a full IT model. Second, the previous attempts are mostly constrained to 2D local domains and as such not only limit the dynamics but may interfere with the background state through impositions created by the selection of regional boundary conditions. In this study, we utilize the newly developed Global ionosphere-thermosphere model with local mesh refinement (GITM-R, Deng et al., 2021) to simulate the first phase of the 2015 Calbuco eruption. The propagation of a simplified forcing function is used for the domain below 100 km altitude, but in this study a fully self-consistent model for IT coupling is utilized to calculate the ionospheric response and for the first time to simulate high resolution meso-scale CVIDs in a global circulation model (GCM), made possible by the local mesh refinement feature. The data-model comparison shows that the observed propagation speed and perturbation amplitude have been well reproduced by the GITM-R simulations. The relative significance of acoustic wave and gravity wave and its dependence on the distance from the eruption location have been examined through both observations and modeling. Meanwhile, some preliminary study indicates that including the ground-coupling process can be a promising way to further improve the data-model comparison in the future.

2 Calbuco 2015 Event Data

The Calbuco volcano is located at ~ 41.3^{o} S, 72.6^{o} W in Southern Chile near the west coast and its vent is approximately 2 km above sea level (Matoza et al., 2018). On April 22-23, 2015, Calbuco erupted following brief seismic activity (<3 hours prior) with two main sub-Plinian phases. The first eruption phase began on April 22nd at 21:04 UT (18:04 LT) and lasted

approximately 1.5 hours based on seismic and visual records. After a nearly 5.5 hour pause, the second eruption phase started on April 23rd at 4:00 UT (1:00 LT) and continued for 6 hours (Matoza et al., 2018; Castruccio et al., 2016). Both phases were categorized as 4/8 on the Volcanic Explosivity Index (VEI), which is in the range typically associated with CVID detection (Astafyeva, 2019). Each Phase injected a plume of mostly andesite particles (~55 wt.% SiO_2) as high as the stratosphere, ~15-17 km altitude, that was then advected northeast (NE) by the local average wind field (Castruccio et al., 2016). Fall deposit and umbrella expansion methods roughly predict bulk injected volumes in the range ~0.27-0.56 km^3, with ~15% being attributed to the first phase and ~85% the second phase (Van Eaton, 2016; Castruccio et al., 2016). Although the second phase was continuous, a notable change in the eruption dynamics occurred ~2 hours after the phase start time with a decrease in the eruption rate, and associated plume height, following the release of pyroclastic density currents from the vent, increasing the electrical activity (Castruccio et al., 2016; Van Eaton et al., 2016). The eruptive column eventually returned to its original height until its abrupt end at ~10:00 UT. Siemo-acoustic analysis of a collocated seismogram and infrasound station < 1000 km from the vent demonstrates a strong cross-correlation in their respective signals indicating air-ground coupling may play a significant role in the propagated air-waves (Matoza et al., 2018).

The ionospheric disturbances induced by the eruptive phases have been analyzed previously (Liu et. al., 2016 and Shults et. al., 2016). CVIDs were examined in both studies by filtering the TEC time series using a bandpass fourth-order zero-phase butter-worth filter with cutoff frequencies at 3 mHz and 8(10) mHz (Liu et al., 2016; Shults et al., 2016). Although they used data from different networks, both showed agreeable results with documented filtered TEC magnitudes of 0.4-0.6 TECU for the first eruption phase and 0.1-0.3 TECU for the second (Liu et

al., 2016; Shults et al., 2016). Liu et al., (2016) estimates the apparent phase speeds as ~800 m/s and ~900 m/s for each respective eruption phase while Shults et al., (2016) estimates ~900 m/s for the first eruptive phase and ~1100-1300 m/s for the second. These discrepancies may be caused by the differences in the corresponding data sets, such as LOS geometry and its relation to CVID wave fronts, or perhaps a methodological contrast when making assumptions about the F2 peak height used in calculations. Both studies report similar spectral content with independent analysis confirming spectral dominance at ~3.7 mHz in Liu et al., (2016) and 3.8-5.2 mHz in Shults et al., (2016)

This study focuses on the first eruption phase since the initial atmospheric state better represents the traditional climatology, whereas propagation of AGWs in the second eruptive phase may be influenced by the first. However, it is worthwhile to mention a brief comparison of the first and second phases in the lower atmosphere, by traditional volcanological techniques, and the IT's response as measured by TEC in the upper atmosphere. Tephra fall deposits, plume expansion, lightning analysis, and seismic/visual records all support that the second eruption phase injected more mass and was far more energetic than the first. Yet, the TEC data would suggest the opposite, with a reported mean TEC response of ~0.45 TECu for the first phase and only ~0.16 TECu for the second phase (Shults et al., 2016). This dichotomy seems to be well explained by the background ionospheric conditions relevant to the timing of each eruption. The first phase occurs around local dusk, having much more electrons to perturb in the north/north-west than the second phase that occurred ~5-6 hours after local sundown. This demonstrates the importance of considering what influences the background ionospheric state when attempting to use TEC observations for ionospheric seismology/volcanology and suggests that a relative

parameter, such as the percentage deviation from the background ionospheric state, could be more valuable especially for attempts at feature extraction.

3 Methodology

3.1 Global Ionosphere-Thermosphere Model with Local-mesh Refinement (GITM-R)

GITM is a 3D non-hydrostatic GCM that solves the Navier-stokes equations for the neutral constituents and simplified MHD for the plasma constituents (Ridley et al., 2006, Deng et al., 2008). GITM uses a stretched altitudinal coordinate with discretization dependent on the scale height (~H/3 in this study) and utilizes two-dimensional domain decomposition that allows for flexibility in specifying the meridional and zonal resolutions. The newly developed version with local-mesh refinement feature (GITM-R) increases this flexibility by allowing layered patches of increased resolution to be imbedded and coupled together (Zhao et al., 2020; Deng et al., 2021). The advantages of using GITM-R for localized meso-scale AGW simulations are threefold:

1) The grid refinement of regional patches allows for extreme flexibility in specifying the resolution in areas of interest and the imbedded, coupled, configuration means regional boundary conditions can be more realistically set (Deng et al., 2021).
2) GITM-R has a self-consistent physics-based description of the coupling between the IT system and solves for neutral and ion densities, dynamics, and temperatures. It includes chemistry, solar and geomagnetic inputs, and viscous and thermal conduction terms for more accurate descriptions of IT phenomena (Ridley et al., 2006; Meng et al., 2022).
3) GITM's numerical configuration allows for non-hydrostatic solutions by explicitly solving the vertical momentum equation. This permits the upward propagation of

acoustic waves and gives a more complete description of high frequency AGWs (Deng et al., 2008; Deng & Ridley, 2014).

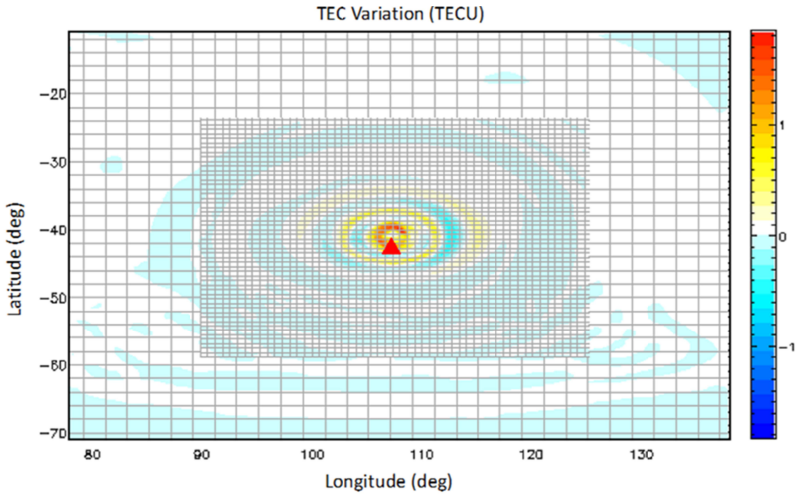

Figure 1. Example of GITM-R run with locally refined domain in the center. Red triangle is Calbuco location. Grid lines are displayed (light grey)

For this simulation a 3-layer imbedded configuration is used and partially shown in ***Figure 1***. The inner most regional layer is centered at the volcano location (41.3° S, 72.6° W) and spans ~15 deg (~1500 km) in either horizontal direction creating a 30° x 30° domain with 0.1° x 0.1° resolution. The second regional domain spans a 60° x 60° square centered at the volcano location and increases the resolution to 0.5° x 0.5°. The domain is completed by the global layer whose resolution is 1.8° in longitude and 1° in latitude. This configuration does not require additional specification of horizontal boundary conditions in the regional domain (Deng et al., 2014, Meng et al., 2015, Lin et al., 2017), a clear advantage to other regionalized simulations.

Although the domain of interest for this simulation is in the middle latitudes the relative magnitude of ionospheric perturbations is highly dependent on the background electron density distribution, therefore the IMF/solar wind conditions from OMNI-web are utilized to drive GITM-R run for ~8 hrs prior to the addition of a volcanic perturbation, to better specify the

249 background state. The other input is solar irradiance given by an f10.7 index with value of 155
250 sfu.

251 GITM-R's vertical extent covers from 100-600 km altitude. At the upper boundary an
252 open condition is used in all layers. During the volcanic event, the lower boundary of the inner
253 most domain is specified using the linear theory of AGWs propagation, details of which are in
254 the next section and appendix.

255 3.2 Source Representation and Propagation to 100 km

256 The atmospheric forcing for a particular volcanic eruption with mass injection rate given
257 by $F_M(t)$ can be estimated, in the linear theory, by the convolution with the atmosphere's
258 response to a step function mass injection (Kanamori et al., 1994). In this model, the
259 atmosphere's response is represented as a single point pressure oscillation described by Equation
260 (1) (Kanamori et al., 1994; Kanamori, 2004).

$$p'(t) = Ae^{\frac{-1}{2H_\rho}}\left\{\delta(t-t_0) - \frac{\omega_a t_0 J_1\left[\omega_a (t^2-t_0^2)^{1/2}\right]}{(t^2-t_0^2)^{1/2}} H(t-t_0)\right\} \quad (1)$$

261 Here, A is a minimum impulse mass injection rate estimated for the first eruption phase as
262 ~6.0e6 kg/s (Van Eaton et al., 2016), H_ρ is the local density scale height (~6 km), δ is the Dirac
263 delta function, H is the Heaviside step function, J_1 is Bessel's function of the first kind (of order
264 1), ω_a is the (local) acoustic cut-off frequency (2.9 mHz, ~5.75 mins), and t_0 is the eruption start
265 time. The above equation is meant to represent the local solution of an isothermal atmosphere to
266 a step change of mass injection. As in previous studies, the time series of the mass injection are
267 presented as a gaussian (derivative) shown in the equation below.

$$F_M(t) = B(t - t_0)e^{\frac{-(t-t_0)^2}{2\sigma_t^2}} \quad (2)$$

where B is an factor used to counter the geometrical spreading of the spherical waves used in the propagation to 100 km, and σ_t is some characteristic time of the eruption chosen here to be 58.5 seconds corresponding to a width of approximately 4-6 mins. In the future this framework would allow studies of specific volcanic events by using data to constrain the mass injection rate, but no such data was available for the Calbuco event. The normalized spectrum of the final forcing function is shown in ***Figure 2***. The forcing function is then propagated to GITM-R's 100 km boundary using spherical waves. By utilizing the assumptions in (Meng, et. al., 2015, 2018, 2022), to relate the horizontal and vertical structures, the AGW dispersion relation can be used to solve for the vertical wavenumber at a given frequency. Further details related to the propagation of the forcing to GITM's lower boundary are given in the appendix.

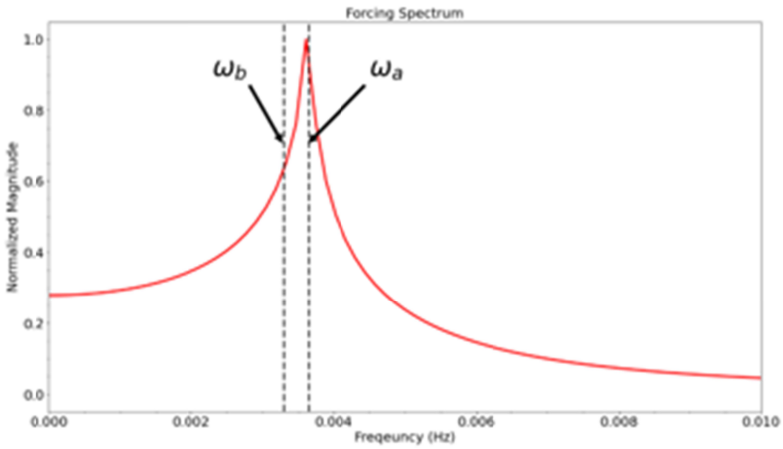

Figure 2. Normalized Forcing spectrum showing clear spectral peak at local acoustic cut-off frequency. Dashed lines mark the local acoustic and buoyant frequencies.

4 Results & Discussion

This section starts with the analysis of GNSS TEC data produced at the MIT Haystack Observatory using global GNSS TEC receiver networks for both phases of the 2015 Calbuco

eruption. Because of limited data availability poleward of the volcano, the measurements north (N) and northeast (NE) of the volcano are shown in Figure 3. Only satellite-receiver pairs with elevation angles greater or equal to 40 degrees were used in the analysis for comparison to GITM-R simulated vertical dTEC. The GNSS vertical TEC data are converted to dTEC by subtracting a smoothed version of the signal using a Savitzky-Golay 1D filter with a window length of 30 minutes (Pauli, et. al. 2020). This Savitzky-Golay filter detrending approach is extensively used to derive TID information; detailed information can be found in e.g., Zhang et al. (2017). This window allows for effectively TID detection without contamination by large sale ionospheric structures. The data are then compared to GITM-R simulation of the first phase of the event driven by the methodology, which is under the direct propagation (DP) assumption and is discussed in section 4.2. Short falls of the methodology and its relevance to recreation of the observed TEC signals are discussed in section 4.3 where a simplified approach to ground-coupled (GC) propagation is tested and compared to GNSS data.

4.1 GNSS observations

The left and right panels of ***Figure 3*** show the detrended GNSS TEC variations for a few of the satellite-receiver (PRN #-site #) pairs in both eruption phases (top for the first phase and bottom for the second). The X-axis shows the UT time and the Y-axis to the right of each of the four data panels shows the amplitude of the detrended GNSS TEC data in TECU (1 TECU ~10^{16} electrons/m^2). The background contour displays the wavelet transform of the times series and provides spectral information as a function of time, measured by the left Y-axis in mHz. The wavelet transform is performed utilizing the python *pywt* package (Gregory et al., 2019) and a complex Morelet wavelet is used for the transform. ***Figure 3*** is oriented such that distance of the GNSS observations increases from top to bottom for each of the four data panels. The distance

from the source for a satellite-receiver pair is determined by the horizontal distance from the source and position along the sub-ionospheric piercing point (SIPP) trajectory where the maximum detrended TECu occurs. The middle panels provide a spatial supplement for the observations showing oversaturated data along the SIPP trajectories for the individual PRN-site pairs. We assume an ionospheric shell height at 350 km for SIPP estimation. Note that the SIPP trajectories include both spatial and temporal variations of the signal.

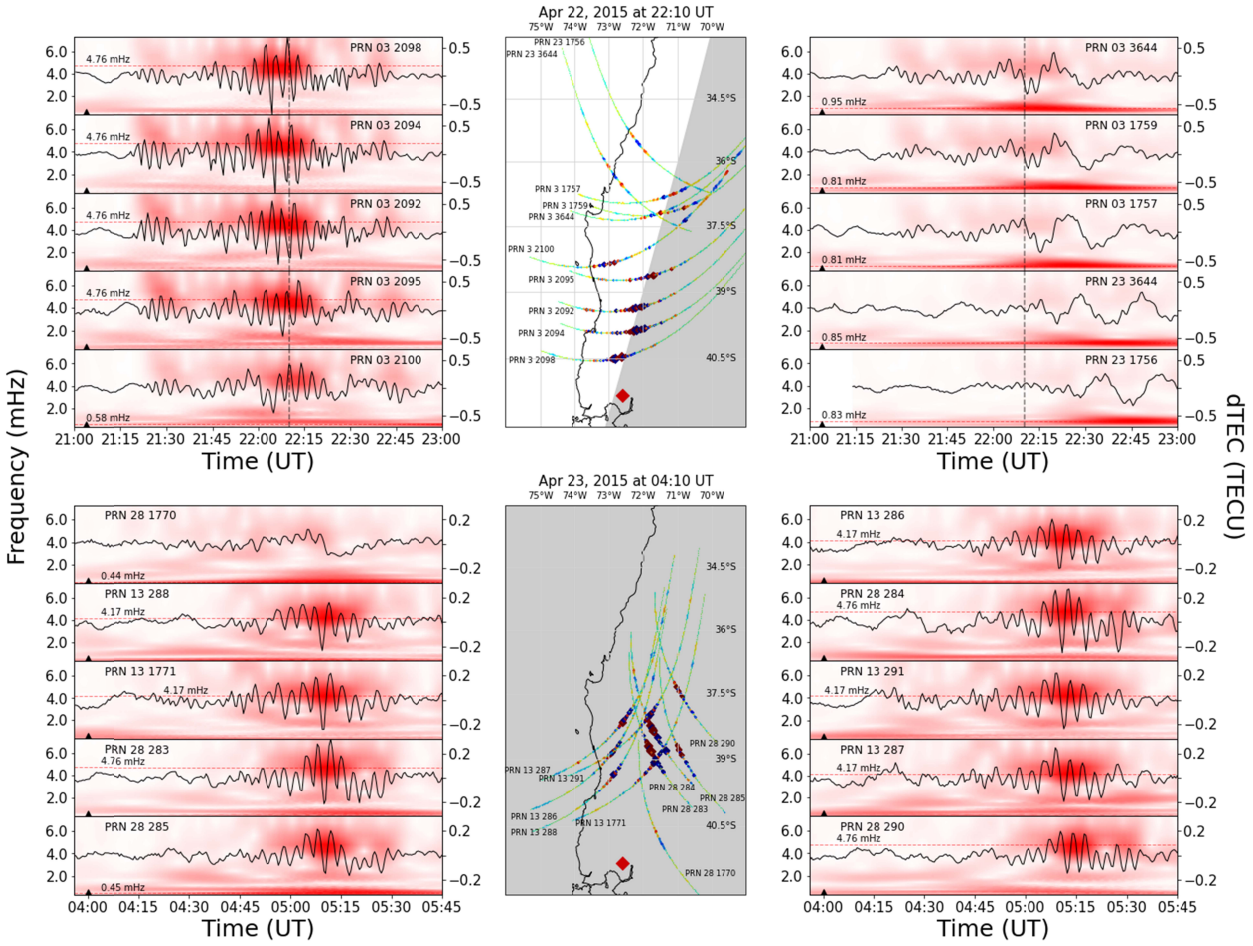

Figure 3. Detrended TEC data for the first (top) and Second (bottom) eruption phase. The background contour represents the corresponding wavelet transform of the displayed time series. Distance from the source increases (down-right) such that the top left is closest to the volcano and bottom right is furthest, in each respective eruption phase panel. The dashed black line represents the frequency with maximum transform amplitude in the time series. Local geography and estimated sub ionospheric piercing point trajectories for GNSS observations are shown in the middle panel. Bright red diamond represents volcano,

trajectory dot size and color are based off oversaturated dTEC magnitude. The black triangle along the time axis represents the start time of the eruption.

For the first eruption phase (Top), the left panel consists of near-field observations (<500 km from the source) and the right panel consists of far-field observations (> 500 km from the source). Focusing on the observations in the near-field (top left panel in ***Figure 3***), the GNSS data (black line) show at least two distinct wave packet structures; one occurring ~8-14 mins after the eruption time and the other ~40-60 mins after, suggesting these may be T1 and T2 disturbances respectively. Both wave packets are quasi-periodic with dominant modes between 4-6 mHz (with an overall maximummax at ~4.67 mHz over the time period; corresponding to a period of ~; 3.5-4 mins) with the maximum magnitude of the detrended TEC being ~0.6 TECU, both of which are well supported by other studies (Shults et al. 2016; Liu et al, 2017). The magnitude of the second wave packet being larger than the first is an interesting observational result and may suggest indirect forcing caused by the eruption, such as turbulence/convection in the plume (Vadas & Liu, 2009; Vadas et al., 2003), leakage of concentrated energy due to atmospheric resonance (Watada & Kanamori, 2010), AGW interaction with the complicated topography of the Andes mountains (Vadas et al., 2019), etc., as a primary mechanism.

For the far-field response to the first eruption (top right panel, ***Figure 3***), the TEC is dominated by a low frequency disturbance showing a spectral peak at ~0.8-0.9- mHz (~17-20 mins). The high-frequency acoustic perturbations are modulated by the low frequency disturbance and reach magnitudes of 0.1-0.3 TECU. It should be noted that the previous publications of Liu et al. (2016) and Shults et al. (2016) do not mention the low frequency mode in their analysis. Potentially, this mode might have been left out of the previous analysis because the filtering techniques in either instance deploy a bandpass filter with a lower cutoff frequency

of 3 mHz. It is not uncommon for such a mode to follow acoustic dominated forcings, such as volcanos and earthquakes, and multiple low-frequency TIDs have beencan be identified in the hours preceding the eruption (Dautermann et al, 2009; Ripepe, et al, 2010; Matsumura et al. 2011; De Angelis et al. 2011; Barfucci et al. 2018; Yue et al. 2022). Althoughand the timing of this event coincides with the passage of the terminator line, caution has to be taken when tracing the origin of this mode. The dashed vertical line in each data panel for the first eruption phase represents the snapshot in time shown by the solar terminator (ST) line in the middle panel. If the ST wave (STW) plays a role, it may be expected that the near and far field observations should be similarly affected, however the near-field observations seem to be less influenced by the low frequency disturbance. The observed distribution perhaps suggests propagation from a localized source below rather than thermal forcing induced by the terminator or TIDs propagating from high-latitudes. However, many factors can contribute to this perceived distribution. For instance, it's possible the relative magnitude contribution of the low frequency mode compared to the acoustic forcing at the relevant time and spatial location may instead result in the perceived distribution. It is known from previous studies that medium scale STW typically has amplitudes of ~0.05-0.5 TECU, and while it is more pronounced at dusk, the timing of this eruption is closer to equinox than solstice and occurred nearer to the solar cycle's maximum than its minimum (Afraimovich, 2008; Forbes et al., 2008). These effects may act to reduce the STW magnitude closer to lower bound and make it hard to identify in the near field where acoustic perturbations may be as large as 6x its amplitude.

Meanwhile, geomagnetic storms can trigger TIDs propagating from high-latitudes to the middle- and low-latitudes (Lyons et al., 2019; Sheng et al. 2020; Zhu et. al. 2022; Zhang et. al., 2022) and may be responsible for the low frequency mode. Although no noticeable

storm/substrom can be identified from the Dst index during the Calbuco volcanic event, as mentioned previously, the detrended TEC shows several TIDs propagating both equatorward and poleward in the hours preceding the eruption. In our methodology, we acknowledge this mode's existence and humor the possibility of it being a low frequency (gravity mode) CVID. We later supplement this view in the comparison to GITM-R simulation (section 4.3), but suggest the reader to be aware of other possibilities.

Most of the results displayed for the second eruption phase (bottom half, ***Figure 3***) are in the mid-field (~400-600 km) from the source. Notably, the GNSS data for the second phase mostly consist of only one distinct quasi-periodic wave packet that occurs ~40-60 mins after the eruption time, a clear T2 type disturbance. Although the eruption in the lower atmosphere lasted nearly 6 hours the upper atmosphere's response only lasts ~1.5 hours, like the first phase. Similarly, the dominant spectral content of the wave packet is nearly identical to the first eruption phase with most energy concentrated into the 4-6 mHz range. It's interesting to note the change in maximum dominant mode associated with PRN 13 opposed to PRN 28 suggesting the direction of SIPP trajectory in this case, moving nearly parallel and anti-parallel respectively, may play a role in the perceived maximum frequency. The TEC response only reached an overall maximum of ~0.2 TECU which agrees with previous publications, but as mentioned early is smaller than that of the first phase. The primary difference in TECU magnitude between the two phases is likely the contrast of the electron number densities between the day side and night side. Absent in the TEC response of the second eruption phase is the gravity mode and initial acoustic wave packet, to which there are some possible explanations. First, it should be noted that the background neutral atmosphere, as well as the local temperature and wind changes caused by the first eruption, may play a significant role in the propagation of AGWs launched from the second

393 eruption phase. In fact, observational imaging of mesospheric airglow from the second eruption
394 phase shows the GW propagation to be altered N-NE of the volcano breaking its nearly
395 concentric pattern (Miller et al. 2015). It is known, by advection of the ash plume, that the
396 average wind field was also directed to N-NE direction and could contribute to the filtering of
397 the GW disturbance which eventually arrive in the ionosphere affecting GNSS observations
398 (Heale & Snively, 2015; Vadas et al., 2009). Second, SIPP trajectories may have been too
399 far/close, at the relevant times, to capture the initial wave packet or GW disturbance, although
400 the total coverage suggests this to be unlikely. Third, Calbuco started a new eruptive phase after
401 43 years, with little precursory activity, meaning the first eruptive phase had to generate an
402 overpressure that split the surrounding earth to open a conduit (Castruccio et al., 2016 , AGU
403 communication). It is perhaps this component of the eruption that induced the initial acoustic
404 wave packet. As such, the absence of these features may suggest a difference in the forcing
405 relevant to the IT system between the two eruption phases. Similarly, the main TEC response in
406 both phases might represent some indirect AGW forcing mechanism and be separate from the
407 initial AGW packet and trailing GW mode, as mentioned previously. As of now, it is unclear as
408 to why the second, more powerful, eruption phase did not exhibit a clear double packet structure
409 or trailing GW disturbance like that of the first phase and the proposed explanations would
410 require additional inquire. Therefore, in our following study, we focus on the first eruption
411 phase.
412

(a)

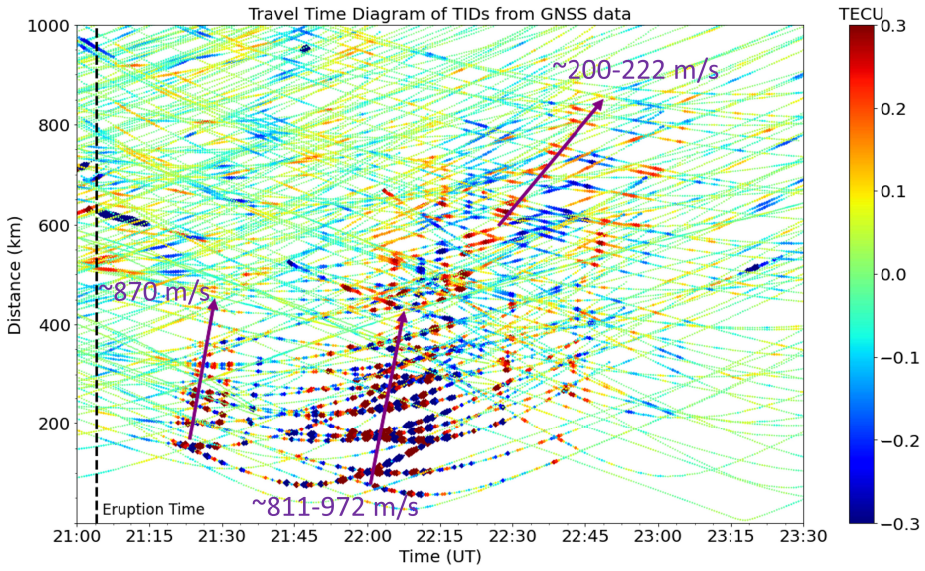

(b)

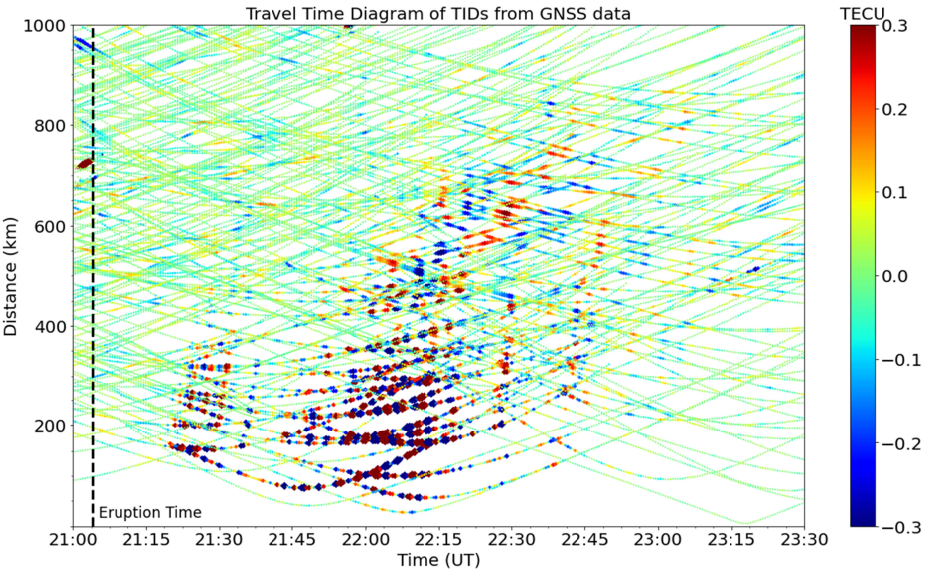

Figure 4. Travel time diagrams for GNSS TEC observations following the first eruption. (a) 30-min SG filter. (b) 15-min SG filter. Dot size is proportional to TECU magnitude, and the color bar is oversaturated to enhance wave visibility.

Figure 4 shows a typical travel time diagrams for the GNSS data during the first eruption phase. The only difference between (a) and (b) is the duration of the SG sliding filter, where (a) is 30 minutes and (b) is 15 minutes. Visible near the source (<500 km) are the high frequency variations associated with the first and second wave packets. The estimated apparent phase speed

from the travel time diagram is ~870 m/s and ~811-986 m/s for the first and second packet respectively. This is in close agreement with those reported by Shults et al. (~911/897 m/s) and Liu et al. (~800 m/s) using the same assumption on the F_2 peak (270 km). At larger distances from the volcano, a lower frequency GW starts to dominate the filtered TEC response and has an estimated apparent phase speed of ~200-222 m/s. The apparent phase speed of ~222 m/s for the gravity mode may be larger than the proposed mesopause bottleneck (Vadas & Azeem, 2021; Vadas et al., 2019;), suggesting the observation may be a secondary GW, if it's origin is the lower atmosphere. However, interaction with the mean flow can shift phase speeds to higher values and primary waves with sufficiently large vertical wavelengths can tunnel through evanescent regions in the lower atmosphere (Walterscheid, et. al. 2003; Heale, et. al. 2022). Numerical results that resolve the lower atmosphere's structure have shown primary waves can reach the thermosphere with phase speeds larger than the proposed bottleneck, even when the calculation accounts for non-isothermal conditions (Gavrilov et. al. 2018; Heale, et. al. 2022).

In **Figure *4*** (b) it's interesting to note the mild suppression of GW signatures in using the smaller sliding window. This allows better visibility of GW induced TID from 400-650 km and may suggest lower frequency components play more of a role at larger distances. Such is expected form the far-field response of relatively localized point sources (Kanimori & Harkrider, 1994; Liu & Yeh, 1970;) and may provide support for the CVID hypothesis.

4.2 Comparison of GITM-R simulations and GNSS observations

For comparison with filtered GNSS observations, GITM-R dTEC is created by subtracting the vTEC of a base run (with no forcing) from the vTEC of a run with forcing. As a result, the GITM-R dTEC only results in the perturbed values and do not include the first order (linear) contributions of the ST wave**. *Figure 5*** shows the direct comparison of the GITM-R simulated

dTEC (blue) and the filtered GNSS observation (black) along the satellite trajectories shown in ***Figure 3*** under the direct propagation (DP) assumption outlined in the methodology/Appendix. The comparison shows decent agreement between simulation and observation for both acoustic and gravity perturbations. Arrival times and perturbation onsets in GITM-R match well to observation near the source but start to differ as the distance of the observations increases. Although the GITM-R dTEC magnitudes underpredict the observations near the source, and overpredict at larger distances, GITM-R reproduces the magnitude distribution as a function of radial distance from the source quite well. Additionally, the relative significance of the acoustic and gravity response is replicated, showing AGW dominant signature in the near-field and dominant GW signatures in far-field. The spectral results for the GITM-R simulation, displayed in the contours of left and right panels in *Figure 5*, show this distribution clearly as well.

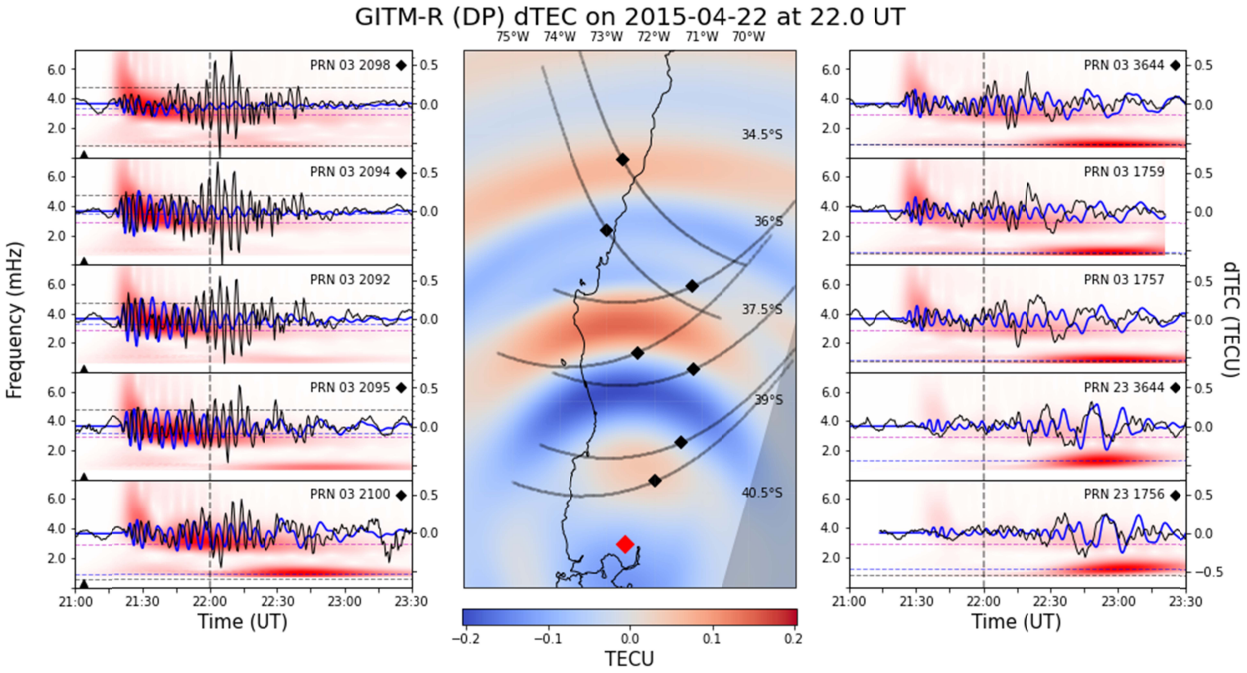

Figure 5. Direct comparison of simulated dTEC (blue) and GNSS observation (black) for the DP case. The format is the same as the top panel in Figure 3. The dashed magenta horizontal line represents the forcing frequency, while the dashed blue and black horizontal lines represent the frequency with maximum transform amplitude for GITM-R simulated and GNSS data respective time series. The dashed vertical line represents the

462 **snapshot in time of the GITM-R simulated dTEC displayed as the color contour in the**
463 **middle panel.**

464 The spectral analysis also shows that the initial wave packet's spectral content matches better to
465 observation, showing dominance in 4-6 mHz range, but as the forcing continues the spectral
466 content of the AGWs starts to approach closer to the forcing frequency (~2.9 mHz; 5.75 mins.),
467 shown by the magenta dashed horizontal line in ***Figure 5***. The dashed blue and black lines
468 represent the spectral maximums found in the GITM-R simulated response and observational
469 GNSS respectively. The initial agreement and later difference may explain why onset and phase
470 of the initial wave packet match so well but start to differ significantly over time and will be
471 further discussed in section 4.3. Noticeable missing from the GITM-R results is the second wave
472 packet in the acoustic mode that represents the main TEC response, although the overall
473 timespan of the perturbation (~ 1.5-2 hrs) seems to match well. As mentioned previously, the
474 double wave packet structure is potentially an indication of dominant modes that together form
475 an envelope in the TEC response. Although the forcing at any point along the lower boundary
476 has two dominant modes (the acoustic forcing frequency and an additional gravity mode,
477 dependent on the propagation angle and the chosen lower atmospheric value [$\bar{\omega}_b sin\theta$]), the
478 current specification is insufficient to recreate the 2-packet structure, because they are too
479 separated in the frequency domain. However, this dominant gravity mode is mostly able to
480 recreate the magnitude, phase, and timespan of the observed GW signatures found in the GNSS
481 data, other than arrival offsets of ~15-30 mins and a more broadly defined spectral packet. Some
482 satellite-receiver pairs find better agreement than others both in apparent phase and magnitude
483 for this mode. Pairs close to the source (left panel, ***Figure 5***) match onset and magnitude of
484 observations of the GW with good agreement, while others, such as those Northeast of the source
485 (Top three right panels, ***Figure 5***), are considerably smaller in magnitude and shifted ~ 30

minutes in time. Interestingly, the farthest pairs (Bottom two right panels, ***Figure 5***), have decent agreement with observations of the GW in magnitude and phase and only ~15 mins of offset.

The location-dependent performance may be due to an effect of the SIPP trajectory motion, e.g. in a direction nearly antiparallel to the GW, or suggest a different forcing mechanism than what is assumed. Meanwhile, the simplified propagation in the lower atmosphere (< 100 km) will also contribute to the discrepancies in GW mode. For example, because the GITM simulated gravity mode is driven directly by the lower boundary forcing at ~100 km altitude, the GW initial properties are strongly under the influence of the assumption of lower atmospheric background parameters. In the current approach the propagated GW signature is unaffected by atmospheric stratification and wind variations in the lower atmosphere, both of which may significantly alter propagation parameters, especially for low frequency waves (Heale, et. al., 2015; Vadas et. al., 2012). Additionally, the primary forcing mechanism may not be the atmosphere's natural buoyant response, which the forcing is meant to represent, and instead be convectively generated in the plume (Vadas, 2013), such as secondary GWs generated by dissipation (Vadas, 2013, Vadas, et al., 2009), be a result of thermal forcing near the solar terminator (Afraimovich, 2008; Liu, et al., 2009; Zhang et. al., 2021), or be TIDs propagating from unrelated sources.

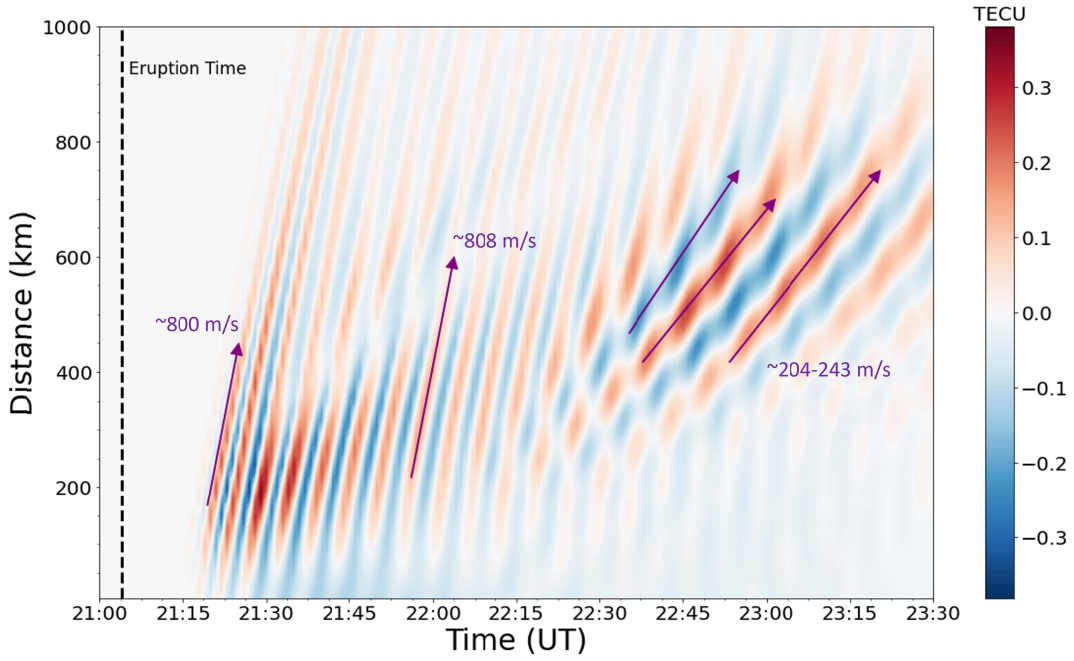

Figure 6. Recreated GITM-R dTEC travel time diagram for the DP case, showing approximated phase speeds.

Figure 6 is a GITM-R reproduction of the travel time diagram shown in ***Figure 4*** . To create the figure, a latitudinal slice is used extending from the volcano location. The AGW packet and trailing GW mode are clearly visible in the GITM-R results and have similar apparent phase speeds to the observations (***Figure 4***) equatorward of the volcano. As mentioned previously, apparent phase speeds of the GNSS data, shown in ***Figure 4***, are estimated to be ~870 m/s and ~811-986 m/s for the first and second acoustic wave packets respectively and ~200-222 m/s for the trailing gravity mode. The estimated equatorward phase speeds for simulated CVIDs associated with the first and second acoustic perturbations are ~800 m/s (~8% diff.) and ~808 m/s (~1-18 % diff.) respectively and the gravity wave perturbations are ~204-243 m/s (~2-19% diff.). A proper comparison of simulated poleward phase speeds cannot be made due to lack of GNSS data coverage, however the GITM-R results predict larger phase speeds for the two modes (Figure not shown). The difference in simulated phase speeds equatorward/poleward of the source may be related to the geomagnetic field orientation (Zettergren & Snively, 2015) or

519 interaction of AGWs with the local neutral mean flow (Heale, et. al. 2022). The GITM-R results
520 also show a latitudinal asymmetry in the dTEC magnitude (not shown in ***Figure 6***). A slight
521 depletion occurs poleward most likely due to the downward transport of ions and electrons along
522 magnetic field lines resulting in a higher recombination rate than plasma pushed equatorward
523 (Meng et. al., 2022).

524 **4.3 Discussion**

525 The GITM-R simulations showed decent agreement with GNSS observations about the first
526 acoustic wave packet and trailing gravity mode when using spherical waves under the direct
527 propagation assumption to force the lower boundary. However, the current forcing methodology
528 misses the second wave packet in its higher spectral content. Three shortcomings of the
529 methodology may provide some explanation for these major differences. The first and most
530 obvious being the oversimplification of the source representation. Our method is purposefully
531 meant to resemble the natural acoustic mode response of the atmosphere in the vicinity of the
532 volcano, however the true near field dynamics are certainly more complicated (Castruccio et al.,
533 2016; Van Eaton et al., 2016). It is not qualitatively known what effect the near field complexity
534 might have on the far-field response; however, the difference between the eruptive phases in the
535 lower atmosphere contrasted with similarities in both waveform and spectral characteristics of
536 the respective ionospheric responses provides evidence that a simplified source could be
537 sufficient to describe the influence on the IT system, at least for this event. Second, the
538 propagation to 100 km uses the assumption of a constant, windless atmosphere, and simplifying
539 the dynamics similar as Meng et al., (2015). Our methodology would not include amplitude
540 changes brought by partial reflection/transmission, tunneling, or doppler shifts associated with
541 background winds (Balachandran, 1968; Brown & Sutherland, 2007; Huang et al., 2010).

Therefore, the energy partitioning of the propagated signal may be over/underestimated for any given mode. Third, only the direct effect of the local atmospheres average response is considered as the forcing in this simulation. Sudden changes in the atmospheric state are sure to produce broad spectral forcing and as such additional AGWs can be produced through secondary mechanisms dependent on the interactions between the volcano-atmosphere-earth. For instance, convective systems can be formed from the cooling of injected gaseous material by the surrounding atmosphere, or as a response to an atmospheric buoyant barrier (such as a temperature inversion layer) in general, and this can result in oscillatory forcing with various periods (Baines & Sacks, 2017). Additionally, the eruption will most likely generate some movement of the earth's surface, either internally or form airwaves impinging on the ground. While the earth and atmosphere have a large impedance, resonant coupling with the lower atmosphere is postulated to sustain amplitudes of long-duration acoustic wave trains as they propagate horizontally and has been used to explain infrasound, seismic, and TEC data related to various eruptions (Schults et. al. 2016; Nakashima et al., 2015; Matoza et al., 2018; Watada & Kanamori, 2010; Heki & Fujimoto, 2022). These secondary coupling/generation mechanisms might provide an explanation for the delay in TEC response between T1 and T2 disturbances. One possible explanation for the second wave packet of the first eruption phase is the localized AGW forcing generated by convection, turbulence, or lightning discharge in the plume, which was known to drift NE direction (Castruccio et al., 2016; Van Eaton et al., 2016), or be related to the leakage of energy from the passage of ground-coupled airwaves (Watada, 1995; Dautermann et. al. 2009; Godin, 2020). Shults et al., (2016) mentioned the spectral peaks of ~3.8-5.2 mHz in the GNSS data are close to the periods of the first trapped atmospheric mode and its successive overtones. Studies have shown for the coupled earth-atmosphere system that these modes are

preferentially excited by above ground sources (Watada, 1995). These modes get reflected in the lower atmosphere due to the vertical temperature/wind structure and create resonance by forming standing wave patterns in the associated waveguides (Watada, 1998; Lognonne et al., 1998; Dautermann et al., 2009; Godin, 2012; Lognonne et al., 2016; Godin, 2020). These waveguides can then efficiently leak energy into the thermosphere.

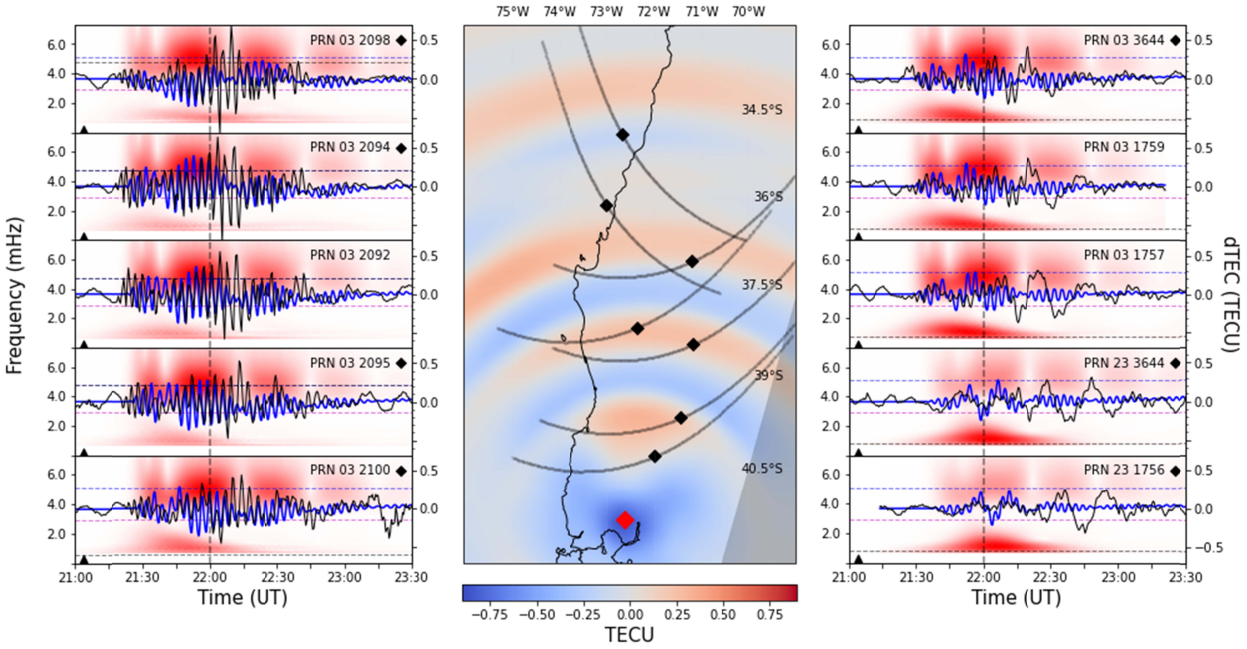

Figure 7. Direct comparison of simulated dTEC (blue) and GNSS observation (black) for the GC case. The format is identical to Figure 5.

To examine the ground-coupled (GC) induced wave properties and whether they could contribute to the observed second wave packet, the propagation methodology is slightly altered to represent a plane wave with an assumed horizontal phase speed dependent on the atmospheric properties along the ground, details of which can be found in the appendix. ***Figure 7*** shows a direct comparison of the GNSS data (black) and GITM-R simulated (blue) dTEC, identical in format to ***Figure 5***. Clearly noticeable in the simulated results is a multi-wave packet structure and tendency toward higher frequency modes in the range 4-6 mHz. While the initial wave packet is shifted by ~10 mins, the arrival time and phase of the second wave packet are in good

agreement with GNSS observations. The duration of the second wave packet in GITM-R is shorter than observation and the associated peak perturbation is shifted ~5 mins. It's clear that the spectral content of the GITM-R results under the GC case matches better than the direct propagation (DP) case, however the dominant modes in the GC case are still insufficient to recreate the exact TEC envelope. As mentioned previously, relaxing the constant background assumption below 100 km might improve the comparison of the simulated result by reducing/enhancing particular modes. Far field AGW magnitudes agree with data and the lower frequency mode of ~1 mHz starts to influence the acoustic signal upon arrival of the second wave packet but opposite in phase, shorter in duration, and smaller in magnitude to observation. This mode is not directly inputted along the lower boundary as forcing at 100 km altitude, as opposed to the DP case, because the low frequency modes ($\boldsymbol{\tau > \tau_a = 5.7\ mins}$) are considered inefficient for coupling with the earth and left out of the reconstruction of the boundary condition (Godin et. al., 2020). Instead, it appears this mode is excited by the lower boundary forcing, in the lower thermosphere, and may be the model's buoyant response. Theoretically, it's expected that spectrally broad pseudo-lamb wave packets can excite GWs in the lower thermosphere and this modeling result seems to agree (Lindzen and Blake, 1972; Watada, 1995; Walterscheid, et. al. 2003; Vadas et al., 2023). It's important to note that psudo-lamb waves, in this context, refer to AGWs whose horizontal propagation is that of the lamb wave but with a non-homogenous lower boundary condition, permitting non-hydrostatic solutions in the vertical ($w \neq 0$) (Walterscheid, et. al. 2003). This distinction is important because the pseudo-lamb wave (from here on just LW) may be the only solution that exists in a real stratified atmosphere (Godin, 2012). This could be expected given that the event occurred over the earth that permitted coupling of the lamb and acoustic branches, leading to the aforementioned acoustic resonance. It

may be interesting to investigate how the LW couples vertically in an event that occurred over the ocean, such as the Tonga event, however observational evidence will have to be heavily supported by proper modeling to discern GWs generated by the passage of the LW (e.g., Zhang et al., 2022) and GWs generated by the breaking of primary GWs (Vadas et al., 2023).

As seen in the snapshot displayed in the middle panels of ***Figure 5*** and ***Figure 7*** the horizontal wavelength of the vdTEC in the GC case is shorter than that of the DP case due to the higher spectral content, as expected. The magnitude of the acoustic forcing directly above the vent appears to result in a TEC depletion, shown in both the middle panel and in the closes displayed SIPP comparison, much larger than that of the DP case, and could explain the sudden depletion found in PRN28 1770 in the second eruption phase (***Figure 3***). Focusing now on the recreated travel time diagram shown in ***Figure 8***, the apparent phase speeds of the first acoustic wave packet is similar to the DP case (~800 m/s, ~8% diff) however the second wave packet now in between the range displayed in the GNSS data (~842 m/s) with a ~4-14% difference to observation. The GW responses shown in ***Figure 8*** have slightly different apparent phase speeds. The initial GW disturbance has the largest phase speed (~312 m/s) while the second and third disturbance are slower at ~285 m/s and ~263 m/s respectively. These estimates also suggest GW generation in the lower thermosphere (Vadas & Azeem, 2021), and the reduction of phase speed is also seen in other numerical simulations of acoustic forcing (Matsumura et al., 2011). These estimates yield ~17-44% diff. to the observational mode and might suggest the responsible mechanism is not the correct forcing the observed GWs.

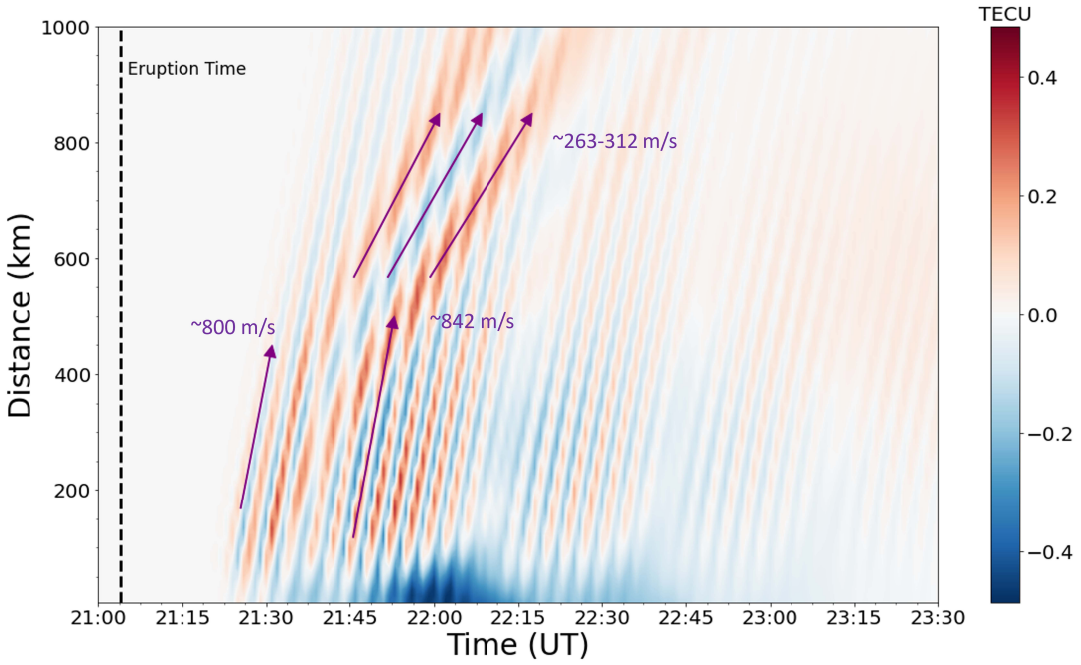

Figure 8. Recreated GITM-R dTEC travel time diagram for the GC case, showing approximated phase speeds.

While the simplified approach outlined above was able to show some improvement in the data-model comparison it is clearly insufficient to reproduce some of the important features of the GNSS TEC data, such as the magnitude of the second wave packet. It is expected that including the vertical temperature structure below 100 km would allow for atmospheric resonance and not only increase the magnitude but help to partition the acoustic energy into dominant modes that produce a better agreement to the envelope of the two-packet structure found in the GNSS observations. A methodology with 2-way coupling of GITM-R and a lower atmosphere model might be needed to fully capture atmospheric resonance as some AGW propagation angles may result in turning point altitudes higher than the lower boundary of GITM (Le Pichon et. al., 2002; De Angelis et al., 2012). Additional complexities such as coupling with solid earth might also improve the data-model comparison. It's likely, for a volcanic eruption, that atmospheric resonance occurs and is needed to fully explain the observed wavefield in the lower atmosphere but relevance to the IT system is still to be determined. Another potential

candidate for formation and magnitude of the second wave packet is the complicated topography created by the Andes mountains just below the SIPP trajectories to the east of the volcano. This topological structure may induce significant interactions of the propagated air waves or concentrate/diffract the coupled seismic waves to generate local enhancements/depletions of energy (Haney et al., 2009). Although many of these features are not included in our current methodology, we believe this work provides a good starting point to further investigate the influence of the coupled earth-atmosphere on the IT system.

5 Conclusion

Observational GNSS TEC data was analyzed for both eruptive phases that occurred during the April 22-23, 2015 Calbuco eruption and the IT response was shown to be of similar duration and spectral dominance as far as ~600 km from the vent (<600 km). The dominant IT response occurred ~30-60 mins after the start of each respective phase and was shown to have high apparent phase speeds (~811-972 m/s), suggesting these TIDs are induced by acoustic waves. The first phase has a notable difference in the observed response due to an initial acoustic wave packet that arrives in the IT much sooner (~8-12 mins) and a low frequency GW mode in the far-field. While GW modes are expected in volcanic events, the timing and location of, as well as background TID activity during, the eruption make it difficult to discern the GW modes origin without detailed modeling of both the source in question and other GW induced ionospheric weather.

For our modeling approach, a simplified spectral model for spherical AGW propagation was used to force the lower boundary of a self-consistent 3D model for IT coupling, GITM-R. It was shown that GITM-R could reproduce important features of the observed GNSS data related to the sub-Plinian eruption of the first phase of the Calbuco 2015 event on April 22nd. In

663 particular, GITM-R was able to reproduce the relative significance of AGW perturbations as a
664 function of radial distance, showing AW dominant perturbations near the source and GW
665 dominant perturbations at further distances. Spectral analysis of the observational GNSS data
666 supports this conclusion, showing dominant perturbations of 3.5-4 mins in the near-field (<500
667 km) and dominant perturbations of 17-20 mins in the far-field (>500 km). The spectral results of
668 the simulated initial acoustic perturbations were close to observation in the frequency domain,
669 with dominance in the 4-6 mHz (2-4 mins) range, while the majority of the AGWs in the
670 timeseries are near the forcing frequency at ~2.9 mHz (~6 mins). At later times and further
671 distances, the simulated GW response has a spectral peak centered close to observation at ~1
672 mHz (16-17 mins) and was broader in spectral space. Although a multiplicative factor was added
673 to the source function (B) to achieve a comparable dTEC magnitude, it was shown the
674 distribution of magnitudes for the initial AW packet and GW also matched to observation quite
675 well, with good agreement near the source and underpredicting GW (overpredicting AW)
676 perturbations at large distances. GITM-R's reproduction of the TTD also showed good
677 agreement with estimated equatorward apparent phase speeds for either mode, with CVIDs
678 associated with the acoustic and gravity wave perturbations having ~4-18 % difference and ~2-
679 19 % difference, respectively.

680 Data-model comparisons were shown to improve when including the ground coupled
681 (GC) specification, but the simplified propagation model was unable to predict relevant
682 magnitudes unless an additional multiplicative factor (q=100) was added. Most notably, the GC
683 specification was able to reproduce the second, larger, wave packet (in the near field) and onset
684 time, maintain spectral dominance in the acoustic range between 4-6 mHz, as in observations,
685 and slightly improve estimated phase speeds of the acoustic wave packets. The overall TEC

envelope in the observation is still not achieved, but the GC specification shows promise, and the results are expected to improve if the lower atmosphere is vertically resolved. Both specifications demonstrated lower frequency perturbations of ~1-2 mHz in the far-field, however the ionospheric response for this mode is quite different because of the assumptions made in the lower boundary forcing. The GW packet response in the GC case had notable differences to the observed GW phase speeds with ~17-44% diff. and might suggest the generation mechanism did not play a significant role in the observed GW mode.

Comparison of the DP and GC cases suggests the initial wave packet might be acoustic waves propagating directly from the source while the second may be formed by the passage of a ground-coupled airwave. For the GW mode, the comparison shows distinct differences in TID propagation and characteristics from the different forcings however, the current forcing specification and modeling environment are not yet sufficient to comment on the origin of the GW mode shown in the GNSS observations. It is clear the current methodology needs to be improved in predicting travel time or phase variations for the GW mode as well as the AWs. A simple combination of the boundary conditions does not result in an improvement to the data-model comparisons, likely because of the difference in dominant modes between the two boundary forcings. Proper combination of the two specifications likely requires resolving the propagation changes induced by the vertical structure below 100 km.

Acknowledgments

This work at UTA was supported by NASA through grants 80NSSC20K1786, 80NSSC22K0061, 80NSSC20K0195, 80GSFC22CA011, and 80NSSC20K0606, and AFOSR through award FA9559-16-1-0364. The authors acknowledge the Texas Advanced Computing Center (TACC, http://www.tacc.utexas.edu) at the University of Texas at Austin for providing HPC resources that have contributed to the research results reported within this paper.

Open Research

GNSS TEC data processing and CEDAR Madrigal open-access database are provided by the MIT Haystack Observatory under support from NSF geospace facility grant AGS-1952737. The original GNSS observations were contributed by numerous community partners. SRZ acknowledges also funding from the AFOSR MURI grant ONR15-FOA-0011, NSF grants AGS-2033787 and AGS-2149698, NASA 80GSFC22CA011 and 80NSSC21K1310. The GNSS data and model outputs are available at https://doi.org/10.5281/zenodo.7787345.

References

Aa, E., Zhang, S.-R., Wang, W., Erickson, P. J., Qian, L., Eastes, R., et al. (2022). Pronounced suppression and X-pattern merging of equatorial ionization anomalies after the 2022 Tonga volcano eruption. Journal of Geophysical Research: Space Physics, 127, e2022JA030527. https://doi.org/10.1029/2022JA030527

Aa, E., Zhang, S.-R., Erickson, P. J., Vierinen, J., Coster, A. J., Goncharenko, L. P., et al. (2022). Significant ionospheric hole and equatorial plasma bubbles after the 2022 Tonga volcano eruption. Space Weather, 20, e2022SW003101. https://doi.org/10.1029/2022SW003101

Afraimovich, E.L. First GPS-TEC evidence for the wave structure excited by the solar terminator. *Earth Planet Sp* **60**, 895–900 (2008). https://doi.org/10.1186/BF03352843

733 A.J. Ridley, Y. Deng, G. Tóth, The global ionosphere–thermosphere model, *Journal of*
734 *Atmospheric and Solar-Terrestrial Physics*, Volume 68, Issue 8, 2006, Pages 839-864, ISSN
735 1364-6826, https://doi.org/10.1016/j.jastp.2006.01.008.
736
737 Astafyeva, E. (2019). Ionospheric detection of natural hazards. *Reviews of Geophysics*, 57, 1265-
738 1288. https://doi.org/10.1029/2019RG000668
739
740 Baines, P. G., & Sacks, S. (2017). The generation and propagation of atmospheric internal waves
741 caused by volcanic eruptions. Atmosphere, 8(3), 60. https://doi.org/10.3390/atmos8030060
742
743 Balachandran, N. K. (1968). Acoustic-gravity wave propagation in a temperature and wind-
744 stratified atmosphere. J. Atmos. Sci., 25, 818-826, 1968
745
746 Barfucci, G., & Ripepe, M. (2018). Dome collapse interaction with the atmosphere. *Geophysical*
747 *Research Letters*, 45, 8923–8930. https://doi.org/10.1029/2018GL078243
748
749 Brown, G. L. & Sutherland, B. R. (2007) Internal wave tunnelling through non-uniformly
750 stratified shear flow, Atmosphere-Ocean, 45:1, 47-56, DOI: 10.3137/ao.v450104
751
752 Cahyadi N. M, Handoko Y. E, Rahayu W. R, and Heki K. Comparison of volcanic explosions in
753 Japan using impulsive ionospheric disturbances. *Earth, Planets and Space* (2021) 73:228
754 https://doi.org/10.1186/s40623-021-01539-5
755

Cahyadi N. M, Rahayu R. W., Heki K., and Nakashima, Y. Harmonic ionospheric oscillation by the 2010 eruption of the Merapi volcano, Indonesia, and the relevance of its amplitude to the mass eruption rate. *Journal of Volcanology ad Geothermal Research*, Volume 405, 1 November 2020, 107047. ISSN 0377-0273, https://doi.org/10.1016/j.jvolgeores.2020.107047.

Cheng, K., & Huang, Y. N. (1992). Ionospheric disturbances observed during the period of Mount Pinatubo eruptions in June 1991. *Journal of Geophysical Research*, 97(A11), 16995–17004. https://doi.org/10.1029/92JA01462

Cappucci, M., Patel, K. and Dauphin, L. Satellite caputres La Palma volcano creating strange cloud ripple. Washington Post, Capital Weather Gang (2021). https://www.washingtonpost.com/weather/2021/10/04/lapalma-volcano-cloud-waves-satellite/

Castruccio, A., Calvero, J., Segura, A., Samaniego, P., Olivier R., Le Pennec, J., Droguett, B. (2016) Eruptive parameters and dynamics of the April 2015 sub-Plinian eruptions of Calbuco Volcano (southern Chile), Bull Volcanol 78:62 doi:10.1007/s00445-016-1058-8

Chimonas G. and Hines C. O. (1970). Atmospheric Gravity Waves Launched by Auroral Currents. Planetary and Space Science, 18, 565-582.

Dautermann, T., Calais, E., & Mattioli, G. S. (2009). Global Positioning System detection and energy estimation of the ionospheric wave caused by the 13 July 2003 explosion of the Soufrière

778 Hills Volcano, Montserrat. Journal of Geophysical Research, 114(B2), B02202.
779 https://doi.org/10.1029/2008JB005722
780
781 De Angelis, S., McNutt, S. R., & Webley, P. W. (2011). Evidence of atmospheric gravity waves
782 during the 2008 eruption of Okmok volcano from seismic and remote sensing observations.
783 *Geophysical Research Letters*, 38, L10303. https://doi.org/10.1029/2011GL047144
784
785 De Angelis, S., Fee, D., Haney, M., and Schneider, D. (2012). Detecting hidden volcanic
786 explosion from Mt. Cleveland Volcano, Alaska with infrasound and ground-coupled airwaves.
787 Geophysical Research Letters, vol. 39, L21312, doi:10.1029/2012GL053635, 2012
788
789 Deng, Y., and A. J. Ridley (2014), Simulation of non-hydrostatic gravity wave propagation in the
790 upper atmosphere, *Ann. Geophys*., 32, 443–447, doi:10.5194/angeo-32-443-2014.
791
792 Deng, Y., A. D. Richmond, A. J. Ridley, and H.-L. Liu (2008), Assessment of the non-
793 hydrostatic effect on the upper atmosphere using a general circulation model (GCM), *Geophys.*
794 *Res. Lett*., 35, L01104, doi:10.1029/2007GL032182.
795
796 Deng Y., Q. Zhu, C. Lin, M. Jin, C. Liu, C. Sheng (2021), Electric field variability and impact on
797 the ionosphere-thermosphere, Book title "Cross-Scale Coupling and Energy Transfer in the
798 Magnetosphere–Ionosphere–Thermosphere System", edited by Y. Nishimura, O.
799 Verkhoglyadova, Y. Deng, and S. Zhang, ISBN: 978-0-12821-366-7, Elsevier publication.
800

Dhomse, S. S., Mann, G. W., Marrero, J. C. A., Shallcross, S. E., Chipperfield, M. P., Carslaw, K. S., Abraham, N. L., Johnson, C. E. (2020). Evaluating the simulated radiative forcings, aerosol properties, and stratospheric warmings from the 1963 Mt Agung, 1982 El Chichon, and 1991 Mt Pinatubo volcanic aerosol clouds. *Atmos. Chem. Phys*., 20, 13627–13654, 2020 https://doi.org/10.5194/acp-20-13627-2020

Forbes, J. M., Bruinsma, S. L., Miyoshi, Y., and Fujiwara, H. (2008), A solar terminator wave in thermosphere neutral densities measured by the CHAMP satellite, Geophys. Res. Lett., 35, L14802, doi:10.1029/2008GL034075.

Godin, O. A. (2012). Acoustic-gravity waves in atmospheric and oceanic waveguides. The Journal of the Acoustical Society of America 132 (2), 657-669

Godin, O. A., Zabotin, N. A., and Zabotin, L. (2020). Atmospheric resonances and their coupling to vibration of the ground and waves in the ocean. Earth, Planets and Space (2020) 72:125 https://doi.org/10.1186/s40623-020-01260-9

Haney M. M., Wijk, K. V., Preston, L. A., Aldridge, D. F., (2009). Observation and Modeling of Source Effects in Coda Wave Interferometry at Pavlof Volcano. Society of Exploration Geophysicists, The Leading Edge, 554-560, doi:10.1190/1.3124930

822 Heale, C. J., Inchin, P. A., & Snively, J. B. (2022). Primary versus secondary gravity wave
823 responses at F-region heights generated by a convective source. Journal of Geophysical
824 Research: Space Physics, 127, e2021JA029947. https://doi.org/10.1029/2021JA029947
825
826 Heale, C. J., and J. B. Snively(2015), Gravity wave propagation through a vertically and
827 horizontally inhomogeneous background wind ,J.Geophys. Res. Atmos.,120, 5931–
828 5950,doi:10.1002/2015JD023505
829
830 Heki, K. (2006). Explosion energy of the 2004 eruption of the Asama Volcano, central Japan,
831 inferred from ionospheric disturbances. Geophysical Research Letters, 33, L14303.
832 https://doi.org/10.1029/2006GL026249
833
834 Heki, K. and Fujimoto, T. (2022). Atmospheric modes excited by the 2021 August eruption of
835 the Fukutoku-Okanoba volcano, Izu-Bonin Arc, observed as harmonic TEC oscillations by
836 QZSS. Earth, Planets, and Space (2022) 74:27, https://doi.org/10.1186/s40623-022-01587-5
837
838 Hines, C. O. (1960). Internal atmospheric gravity waves at ionospheric heights. Canadian Journal
839 of Physics, 38(11), 1441– 1481. https://doi.org/10.1139/p60-150
840
841 Huang, K. M., Zhang, S. D., and Yi, F. (2010), Reflection and transmission of atmospheric
842 gravity waves in a stably sheared horizontal wind field, J. Geophys. Res., 115, D16103,
843 doi:10.1029/2009JD012687.
844

Inchin, Pavel A., "Atmospheric and Ionospheric Responses to Acoustic and Gravity Waves Driven by Earthquakes and Tsunamis" (2020). Dissertations and Theses. 523.

Kanamori, H., Mori, J., & Harkrider, D. G. (1994). Excitation of atmospheric oscillations by volcanic eruptions. Journal of Geophysical Research, 99(B11), 21,947– 21,961. https://doi.org/10.1029/94JB01475

Klobuchar, J. A. (1985), Ionospheric time delay effects on earth space propagation, in Handbook of Geophysics and the Space Environment, edited by A. S. Jursa chap. 10.8, pp. 1084–1088, U.S. Air Force, Washington, D. C

Komjathy, A., D. A. Galvan, P. Stephens, et al. (2012), Detecting ionospheric TEC perturbations caused by natural hazards using a global network of GPS receivers: The Tohoku case study, Earth Planets Space, 64, 24, doi:10.5047/eps.2012.08.003.

Kurokawa, K. A. and Ichihara, M. (2020). Identification of infrasonic and seismic components of tremors in single-station records: application to the 2013 and 2018 events at Ioto Island, Japan. Earth, Planets and Space (2020) 72:171 https://doi.org/10.1186/s40623-020-01302

Koucká Knížová P, Laštovicka J, Kouba D, Mošna Z, Podolská K, Potužníková K, Šindelárová T, Chum J and Rusz J (2021) Ionosphere Influenced From Lower-Lying Atmospheric Regions. Front. Astron. Space Sci. 8:651445. doi: 10.3389/fspas.2021.651445

868 Le Pichon, A., Guilbert, J., Vega, A., Garcés, M., and Brachet, N., Ground-coupled air waves
869 and diffracted infrasound from the Arequipa earthquake of June 23, 2001, Geophys. Res. Lett.,
870 29(18), 1886, doi:10.1029/2002GL015052, 2002.
871
872 Lindstrom, S. (2015). Gravity Waves Associated with Calbuco Volcanic Eruption. CIMSS
873 Satellite Blog, University of Wisconsisn-Madison. https://cimss.ssec.wisc.edu/satellite-
874 blog/archives/18174
875
876 Liu, C. H. & Yeh, K. C. (1971) Excitation of acoustic-gravity waves in an
877 isothermal atmosphere, Tellus, 23:2, 150-163, DOI: 10.3402/tellusa.v23i2.10375
878
879 Liu, H., H. Lu¨hr, and S. Watanabe (2009), A solar terminator wave in thermospheric wind and
880 density simultaneously observed by CHAMP, Geophys. Res. Lett., 36, L10109,
881 doi:10.1029/2009GL038165.
882
883 Liu, L., Morton, Y. J., Cheng, P.-H., Amores, A., Wright, C. J., & Hoffmann, L. (2023).
884 Concentric traveling ionospheric disturbances (CTIDs) triggered by the 2022 Tonga volcanic
885 eruption. Journal of Geophysical Research: Space Physics, 128, e2022JA030656.
886 https://doi.org/10.1029/2022JA030656
887
888 Liu, X., Zhang, Q., Shah, M., Hong, Z., Atmospheric-ionospheric disturbances following the
889 April 2015 Calbuco volcano from GPS observations, Advances in Space Research (2017), doi:
890 http://dx.doi.org/10.1016/j.asr.2017.07.007

Lognonné, P., Clévédé, E., Kanamori, H. (1998). Computation of seismograms and atmospheric oscillation by normal-mode summation for a spherical earth model with realistic atmosphere. Geophys. *J. Int*. (1998) 135, 388-406

Lognonné, P., Karakostas, F., Rolland, L., and Nishikawa, Y. (2016). Modeling of atmospheric-coupled Rayleigh waves on planets with atmosphere: From Earth observation to Mars and Venus perspectives. *The Journal of the Acoustical Society of America* 140, 1447 (2016); doi: 10.1121/1.4960788

Lyons, L. R., Nishimura, Y., Zhang, S. R., Coster, A. J., Bhatt, A., Kendall, E., & Deng, Y. (2019). Identification of auroral zone activity driving large-scale traveling ionospheric disturbances. Journal of Geophysical Research: Space Physics, 124, 700–714. https://doi.org/ 10.1029/2018JA025980

Miller, D. S. , Straka III, C. W, Jia, Y., Smith, M. S., Alexander, J. M., Hoffmann, L., Setvak, M. and Partain, T. P. Upper atmospheric gravity wave details revealed in nightglow satellite imagery. Proceedings of the National Academy of Sciences (2015), E6728–E6735, www.pnas.org/cgi/doi/10.1073/pnas.1508084112

Matoza, R. S., Fee, D., Green, D. N., Le Pichon, A., Vergoz, J., Haney, M. M., et al. (2018). Local, regional, and remote seismo-acoustic observations of the April 2015 VEI 4 eruption of

913 Calbuco volcano, Chile. Journal of Geophysical Research: Solid Earth, 123, 3814–3827.
914 https://doi.org/10.1002/2017JB015182
915
916 Matoza, R. S. et al. (2022). Atmospheric waves and global seismoacoustic observations of the
917 January 2022 Hunga Tonga eruption. Science 10.1126/science.abo7063 (2022).
918
919 Matsumura, M., Saito, A., Iyemori, T., Shinagawa, H., Tsugawa, T., Otsuka Y., Nishioka, M.,
920 and Chen, C. H. (2011). Numerical simulations of atmospheric waves excited by the 2011 of the
921 Pacific coast of Tohoku Earthquake. Earth Planets Space, 60, 885-889, 2011
922
923 Mauk, F. J. Utilization of seismically recorded infrasonic and acoustic signals to monitor
924 volcanic explosions: The El Chichon Sequence 1982—A case study. J. Geophys. Res. 88,
925 10,385–10,401, doi: 10.1029/JB088iB12p10385 (1983).
926 Ripepe, M., Barfucci, G., De Angelis, S. et al. Modeling Volcanic Eruption Parameters by Near-
927 Source Internal Gravity Waves. Sci Rep 6, 36727 (2016). https://doi.org/10.1038/srep36727
928
929 Meng, X., Komjathy, A., Verkhoglyadova, O. P., Yang, Y.-M., Deng, Y., and Mannucci, A. J.
930 (2015), A new physics-based modeling approach for tsunami-ionosphere coupling, Geophys.
931 Res. Lett., 42, 4736–4744, doi:10.1002/2015GL064610.
932
933 Meng, X., Ravanelli, M., Komjathy, A., Verkhoglyadova, O. P. (2022). On the North-South
934 Asymmetry of Co-Seismic Ionospheric Disturbances During the 16 September 2015 Illapl M8.3
935 Earthquake. Geophys. Res. Lett., 49, issue 8. https://doi.org/10.1029/2022GL098090

Meng, X., Verkhoglyadova, O. P., Komjathy, A., Savastano, G., & Mannucci, A. J. (2018). Physics-based modeling of earthquake-induced ionospheric disturbances. Journal of Geophysical Research: Space Physics, 123, 8021–8038. https://doi.org/10.1029/2018JA025253

Nakashima, Y., Heki, K., Takeo, A., Cahyadi N. M., Aditiya, A., Yoshizawa, K. (2016). Atmospheric resonant oscillations by the 2014 eruption of the Kelud volcano, Indonesia, observed with the ionospheric total electron contents and seismic signals. Elsevier B.V Earth and Planetary Science Letters 434 (2016)112–116. http://dx.doi.org/10.1016/j.epsl.2015.11.029

Pauli Virtanen, Ralf Gommers, Travis E. Oliphant, Matt Haberland, Tyler Reddy, David Cournapeau, Evgeni Burovski, Pearu Peterson, Warren Weckesser, Jonathan Bright, Stéfan J. van der Walt, Matthew Brett, Joshua Wilson, K. Jarrod Millman, Nikolay Mayorov, Andrew R. J. Nelson, Eric Jones, Robert Kern, Eric Larson, CJ Carey, İlhan Polat, Yu Feng, Eric W. Moore, Jake VanderPlas, Denis Laxalde, Josef Perktold, Robert Cimrman, Ian Henriksen, E.A. Quintero, Charles R Harris, Anne M. Archibald, Antônio H. Ribeiro, Fabian Pedregosa, Paul van Mulbregt, and SciPy 1.0 Contributors. (2020) SciPy 1.0: Fundamental Algorithms for Scientific Computing in Python. *Nature Methods*, 17(3), 261-272.

Pradipta, R., Carter, B. A., Currie, J. L., Choy, S., Wilkinson, P., Maher, P., & Marshall, R. (2023). On the propagation of traveling ionospheric disturbances from the Hunga Tonga-Hunga

958 Ha'apai volcano eruption and their possible connection with tsunami waves. Geophysical
959 Research Letters, 50, e2022GL101925. https://doi.org/10.1029/2022GL101925
960
961 Ripepe, M., De Angelis, S., Lacanna, G. & Voight, B. Observation of infrasonic and gravity
962 waves at Soufrière Hills Volcano, Montserrat. Geophys. Res. Lett. 37, L00E14, doi:
963 10.1029/2010GL042557 (2010).
964
965 Sheng, C., Deng, Y., Zhang, S.-R., Nishimura, Y., & Lyons, L. R. (2020). Relative contributions
966 of ion convection and particle precipitation to exciting large-scale traveling atmospheric and
967 ionospheric disturbances. Journal of Geophysical Research: Space Physics, 125,
968 e2019JA027342. https://doi.org/0.1029/2019JA027342
969
970 Shestakov, N.; Orlyakovskiy, A.; Perevalova, N.; Titkov, N.; Chebrov, D.; Ohzono, M.;
971 Takahashi, H. Investigation of Ionospheric Response to June 2009 Sarychev Peak Volcano
972 Eruption. Remote Sens. 2021, 13, 638. https:// doi.org/10.3390/rs13040638
973
974 Shinagawa H. Iyemori T., Saito S., and Maruyama T. A numerical simulation of ionospheric and
975 atmospheric variations associated with the Sumatra earthquake on December 26, 2004. Earth
976 Planets Space, 59, 1015-1026 (2007).
977
978 Shults, K., E. Astafyeva, and S. Adourian (2016), Ionospheric detection and localization of
979 volcano eruptions on the example of the April 2015 Calbuco events, J. Geophys. Res. Space
980 Physics, 121, 10,303–10,315, doi:10.1002/2016JA023382.

Sysel, P. and Rajmic, P. (2012). Goertzel algorithm generalized to non-integer multiples of fundamental frequency. EURASIP Journal on Advances in Signal Processing 2012, 2012:56 http://asp.eurasipjournals.com/content/2012/1/56

Vadas, S. L. (2013), Compressible *f*-plane solutions to body forces, heatings, and coolings, and application to the primary and secondary gravity waves generated by a deep convective plume, *J. Geophys. Res. Space Physics*, 118, 2377– 2397, doi:10.1002/jgra.50163.

Vadas, S. L., & Azeem, I. (2021). Concentric secondary gravity waves in the thermosphere and ionosphere over the continental United States on 25-26 march 2015 from deep convection. *Journal of Geophysical Research: Space Physics*, *126*, e2020JA028275. https://doi.org/10.1029/2020JA028275

Vadas, S. L., Fritts, D. C., & Alexander, M. J. (2003). Mechanism for the generation of secondary waves in wave breaking regions. *Journal of the Atmospheric Sciences*, *60*, 194–214. https://doi.org/10.1175/1520-0469(2003)060<0194:mftgos>2.0.co;2

Vadas, S. L., & Liu, H. L. (2009). Generation of large scale gravity waves and neutral winds in the thermosphere from the dissipation of convectively generated gravity waves. *Journal of Geophysical Research*, *114*. https://doi.org/10.1029/2009ja014108

1003 Vadas, S. L., Becker, E., Figueiredo, C., Bossert, K., Harding, B. J., & Gasque, L. C. (2023).
1004 Primary and secondary gravity waves and large-scale wind changes generated by the Tonga
1005 volcanic eruption on 15 January 2022: Modeling and comparison with ICON-MIGHTI winds.
1006 Journal of Geophysical Research: Space Physics, 128, e2022JA031138.
1007 https://doi.org/10.1029/2022JA031138
1008
1009 Vadas, S. L., Figueiredo, C., Becker, E., Huba, J. D., Themens, D. R., Hindley, N. P., Galkin, I.,
1010 Bossert, K. (2023). Traveling ionospheric disturbances induced by the secondary gravity waves
1011 from the Tonga eruption on 15 January 2022: Modeling with MESORAC/HIAMCM/SAMI3 and
1012 comparison of GPS/TEC and ionosonde data. *Journal of Geophysical Research, XXX.*
1013
1014 Vadas, S. L., and Nicolls, M. J. (2012), The phases and amplitudes of gravity waves propagating
1015 and dissipating in the thermosphere: Theory, J. Geophys. Res., 117, A05322,
1016 doi:10.1029/2011JA017426
1017
1018 Vadas, S. L., Xu, S., Yue, J., Bossert, K., Becker, E., & Baumgarten, G. (2019). Characteristics
1019 of the quiet-time hot spot gravity waves observed by
1020 GOCE over the southern Andes on 5 July 2010. *Journal of Geophysical Research: Space*
1021 *Physics*, *124*. https://doi.org/10.1029/2019JA026693
1022
1023 Vadas, S. L., Yue, J., She, C.-Y., Stamus, P. A., & Liu, A. Z. (2009). A model study of the
1024 effects of winds on concentric rings of gravity waves

from a convective plume near Fort Collins on 11 May 2004. *Journal of Geophysical Research*, *114*(D6). https://doi.org/10.1029/2008JD01

Van Eaton, A. R. , Amigo, A., Bertin, D., Mastin, L. G., Giacosa, R. E., Gonzalez, J., Valderrama, O., Fontijn, K., and Behnke, S. A. (2016), Volcanic Lightning and plume behavior reveal evolving hazards during the April 2015 eruption of Calbuco volcano, Chile, Geophys. Res. Lett., 43, 3563-3571, doi:10.1002/2016GL068076

Walterscheid, R. L., and J. H. Hecht, A reexamination of evanescent acoustic-gravity waves: Special properties and aeronomical significance ,J. Geophys. Res.,108(D11), 4340, doi:10.1029/2002JD002421, 2003.

Watada, S. (1995). Part I: Near-source Acoustic Coupling between the Atmosphere and the Solid Earth During Volcanic Eruptions (Thesis). California Institute of Technology

Watada, S. (2009). Radiation of acoustic and gravity waves and propagation of boundary waves in the stratified fluid from a time-varying bottom boundary. J. Fluid Mech. (2009), vol. 627, pp. 361–377. c 2009 Cambridge University Press, doi:10.1017/S0022112009005953

Watada, S., and Kanamori, H. (2010), Acoustic resonant oscillations between the atmosphere and the solid earth duringthe 1991 Mt. Pinatubo eruption, J. Geophys. Res., 115, B12319, doi:10.1029/2010JB007747.

1048 Yue, J., Miller, S. D., Straka III, W. C., Noh, Y.-J., Chou, M.-Y., Kahn, R., & Flower, V. (2022).
1049 La Soufriere volcanic eruptions launched gravity waves into space. Geophysical Research
1050 Letters, 49, e2022GL097952. https://doi. org/10.1029/2022GL097952
1051
1052 Zettergren, M. D., and J. B. Snively (2015), Ionospheric response to infrasonic-acoustic waves
1053 generated by natural hazard events, J. Geophys. Res. Space Physics, 120, 8002–8024,
1054 doi:10.1002/2015JA021116.
1055
1056 Zhang, K.; Wang, H., Zhong, Y., Xia, H., Qian, C. The Temporal Evolution of F-Region
1057 Equatorial Ionization Anomaly Owing to the 2022 Tonga Volcanic Eruption. Remote Sens.
1058 2022, 14, 5714. https://doi.org/10.3390/rs14225714
1059
1060 Zhang, S., Erickson, P. J., Gasque, L. C., Aa, E., Rideout, W., Vierinen, J., Goncharenko, L. P. &
1061 Coster, A. J. (2021). Electrified Post sunrise Ionospheric Perturbations at Millstone Hill.
1062 Geophysical Research Letters, 48(18), e2021GL095151. https://doi.org/10.1029/2021gl095151
1063
1064 Zhang, S.-R., Nishimura, Y., Erickson, P. J., Aa, E., Kil, H., Deng, Y., Thomas, E. G., Rideout,
1065 W., Coster, A. J., Kerr, R. & Vierinen, J. (2022). Traveling Ionospheric Disturbances in the
1066 Vicinity of Storm-Enhanced Density at Midlatitudes. Journal of Geophysical Research: Space
1067 Physics, 127(8), e2022JA030429. https://doi.org/10.1029/2022ja030429
1068
1069 Zhang S.-R., Vierinen J., Aa E., Goncharenko LP., Erickson PJ., Rideout W., Coster AJ. and
1070 Spicher A. (2022). 2022 Tonga Volcanic Eruption Induced Global Propagation of Ionospheric

Disturbances via Lamb Waves. Front. Astron. Space Sci. 9:871275.
doi:10.3389/fspas.2022.871275

Zhao, Y., Y. Deng, J. Wang, S. Zhang and C. Lin, (2020), Tropical cyclone induced gravity wave perturbations in the upper atmosphere: GITM-R simulations, J. Geophys. Res.: Space Physics, 125, e2019JA027675. https://doi.org/10.1029/2019JA027675.

Zhu Q, Lu G and Deng Y (2022) Low and Mid-Latitude Ionospheric Response to the 2013 St. Patrick's Day Geomagnetic Storm in the American Sector: Global Ionosphere Thermosphere Model Simulation. Front. Astron. Space Sci. 9:916739.doi: 10.3389/fspas.2022.916739

APPENDIX A

As mentioned in the main text, GITM-R's lower boundary is at 100 km altitude and there is a need to represent the propagation of the forcing signal to the lower boundary. First, to represent the atmosphere below 100 km a local MSIS profile is used to calculate an altitudinal average of basic atmospheric properties of interest ($\bar{\rho}, \bar{T}, \frac{d\bar{\rho}}{dz}$) which are then used to calculate other atmospheric properties of interest (such as $\bar{\omega}_a^2, \bar{\omega}_b^2, \bar{c}^2$). The purpose of this methodology is to skew the average atmospheric properties to better represent important characteristics, such as $\bar{\omega}_a^2 \; and \; \bar{\omega}_b^2$, close to the vent altitude (~2 km). Dynamics of AGWs are represented using the linearized, density scaled, Euler equations in an isothermal (constant background) atmosphere in the absence of wind, shown below.

$$\frac{\partial \hat{\rho}}{\partial t} + \rho_0 \left(\boldsymbol{\nabla} \cdot \hat{\boldsymbol{v}} - \frac{\hat{w}}{2\bar{H}_\rho} \right) = 0$$

$$\frac{\partial \hat{u}}{\partial t} + \frac{1}{\rho_0}\frac{\partial \hat{P}}{\partial x} = 0$$

$$\frac{\partial \hat{w}}{\partial t} + \frac{\bar{g}}{\rho_0}\hat{\rho} + \frac{1}{\rho_0}\left(\frac{\partial \hat{P}}{\partial z} - \frac{\hat{P}}{2\bar{H}_\rho}\right) = 0$$

$$\frac{\partial \hat{P}}{\partial t} - \bar{c}^2\frac{\partial \hat{\rho}}{\partial t} + \rho_0\beta\hat{w} = 0$$

1092 Where ρ_0 is the neutral density along the ground (~1.11 Pa), $\bar{H}_\rho = -\frac{1}{\bar{\rho}}\frac{\bar{d\rho}}{dz}$, $\bar{c}^2 = \gamma R\bar{T}$, and

1093 $\beta = \frac{\bar{c}^2}{\bar{H}_\rho} - \bar{g}$. The equation set is formulated with $\hat{u}$ as a horizontal track velocity which can be

1094 generalized to three dimensions (Vadas et. al. 2011). Taking the Fourier transform of the

1095 equation set ($\tilde{x} = \int \hat{x} e^{i(\omega t - \boldsymbol{k}\cdot\boldsymbol{r})} d\boldsymbol{r}dt$, $\boldsymbol{r} = (x, z), \boldsymbol{k} = (k, m)$) gives the algebraic system,

$$\begin{bmatrix} i\omega^2 & -\rho_0\alpha\omega & -ik^2 \\ \bar{g} & i\rho_0\omega & -\alpha \\ -i\bar{c}^2\omega & \rho_0\beta & i\omega \end{bmatrix}\begin{bmatrix} \tilde{\rho} \\ \tilde{w} \\ \tilde{p} \end{bmatrix} = 0 \quad (4)$$

1096 where $\alpha = im + \frac{1}{2H_\rho}$. The determinate of the above system, set to zero, gives the well know

1097 dispersion relation for AGWs where solving for the vertical wavenumber gives,

$$m^2 = \frac{\omega^2 - \bar{\omega}_a^2}{\bar{c}^2} - k^2\frac{\omega^2 - \bar{\omega}_b^2}{\omega^2}. \quad (3)$$

.

1098 Here ω is the angular frequency, m is the vertical wavenumber, and k is the horizontal track

1099 wavenumber, and $\bar{\omega}_a^2 \equiv \frac{\bar{c}^2}{4\bar{H}_\rho^2}$, $\bar{\omega}_b^2 \equiv \frac{\bar{g}\beta}{\bar{c}^2}$ define the acoustic cut-off and buoyancy frequencies

1100 respectively. When $m^2 > 0$ the positive solution is used for acoustic frequencies ($\omega > \omega_a$) and

1101 the negative solution for gravity frequencies ($\omega < \omega_b$) to give an upward propagating mode

1102 (Godin, O. A. 2020; Watada, S. 2009). To use the dispersion relation and Fourier representation,

1103 the spectral method developed in (Meng, X. et. al. 2015, 2018, 2022) is used to propagate the

1104 forcing spectrum using spherical waves under the assumption $k^2 = m^2 tan^2\theta$ where θ is the

1105 propagation angle measured from a vertical axis extending from the source. If $\boldsymbol{r} = (r_h, z - z_s)$ is

1106 the separation vector between any point along GITM-Rs lower boundary (x_b, y_b, z_b) and the

1107 source (x_s, y_s, z_s) , then $tan^2\theta = \frac{r_h^2}{(z-z_s)}$ and (3) can be used to calculate the vertical

1108 wavenumber. The AGW forcing to GITM-R is then given by spectral reconstructions

$$w = \left(\frac{\rho_{0km}}{\rho_{100km}}\right)^{1/2} \frac{1}{2\pi r} \int G_P^w \tilde{P} e^{i(\boldsymbol{k}\cdot\boldsymbol{r}-\omega t)} d\omega \quad (4)$$

$$(u, v) = \left(\frac{\rho_0}{\rho_{100km}}\right)^{1/2} \frac{1}{2\pi r} \int \frac{(k_x, k_y)}{\rho_0 \omega} \tilde{P} e^{i(\boldsymbol{k}\cdot\boldsymbol{r}-\omega t)} d\omega \quad (5)$$

$$T = \left(\frac{\rho_{0km}}{\rho_{100km}}\right)^{1/2} \frac{1}{2\pi r} \int \frac{\left(1 - \bar{T} R G_P^\rho\right)}{\rho_0 R} \tilde{P} e^{i(\boldsymbol{k}\cdot\boldsymbol{r}-\omega t)} d\omega \quad (6)$$

1109

1110 where $\tilde{P}$ is the Fouier transform of the forcing signal, r is the separation vector between the

1111 source and the boundary point of interest, $\boldsymbol{k} = (|m|tan\theta, m)$ is the assumed resonant k-vector

1112 for the given point, and G_P^w and G_p^ρ are the solutions to

$$\begin{bmatrix} i\omega^2 & -\rho_0 \alpha \omega \\ \bar{g} & i\rho_0 \omega \\ -i\bar{c}^2 \omega & \rho_0 \beta \end{bmatrix} \begin{bmatrix} G_P^\rho \\ G_P^w \end{bmatrix} = \begin{bmatrix} ik^2 \\ \alpha \\ -i\omega \end{bmatrix}.$$

1113 via left psudo-inverse. The Fourier decomposition/reconstruction is performed using 5000

1114 equally partitioned frequencies in the range [0,40] mHz. The decomposition/reconstruction is

1115 done bin-wise using the non-integer generalized Goertzel algorithm (Sysel & Rajmic, 2012).

To test the hypothesis that the second wave packet is evidence of local forcing due to ground-coupled airwaves, the propagation methodology is slightly altered. Instead of making an assumption on the horizontal track wavenumber $\boldsymbol{k}$, an assumption is made on the horizontal track phase speed ($\boldsymbol{v_s = \frac{\omega}{k}}$) following (Kurokawa, K. A. and Ichihara, M. 2020) as

$$v_s = \frac{c_g}{sin\theta_g}. \quad (7)$$

Where $\boldsymbol{c_g = 334\ m/s}$ is the sound speed along the ground, calculated by the MSIS profile and supported by infrasound records (Matoza, R. S. et. al. 2018), and $\boldsymbol{\theta_g}$ is the ground strike angle measured from the vertical. The strike angle $\boldsymbol{\theta_g}$ is found for each angular frequency by first assuming direct propagation to the point $(\boldsymbol{r_h, -z_s})$, using the defined spatial structure, assuming downward energy propagation ($\boldsymbol{\frac{\partial \omega}{\partial m} < 0}$), to compute vertical and horizontal group velocities $\left(\boldsymbol{v_{gx} = \frac{\partial \omega}{\partial k}, v_{gz} = \frac{\partial \omega}{\partial m}}\right)$, then calculating the radial separation between the ground strike point and the volcano's vent as $\boldsymbol{r_g = \frac{-z_s v_{gx}}{v_{gz}}}$. The strike angle can then be expressed as,

$$\theta_g = sin^{-1}\left(\frac{r_g}{\sqrt{r_g^2 + z_s^2}}\right). \quad (8)$$

Note as $\boldsymbol{r_g \gg z_s}$, $\boldsymbol{sin\theta_g \rightarrow 1}$ and $\boldsymbol{v_s \rightarrow c_g}$ representing a kind of lamb mode. The desired changes come with an additional factor for dispersion under direct propagation to $\boldsymbol{(r_g, -z_s)}$ defined as $\boldsymbol{\delta_s = \frac{e^{i(k_h r_g - m z_s)}}{\sqrt{r_g^2 + z_s^2}}}$ where $\boldsymbol{k}$ is calculated on the direct propagation (DP) assumption and the denominator accounts for geometric spreading. An example for the reconstructed vertical velocity at GITM-R's lower boundary is,

$$\boldsymbol{w = \left(\frac{\rho_{0km}}{\rho_{100km}}\right)^{1/2} \frac{q}{2\pi} \int G_P^w \delta_s \tilde{P} e^{i[k\cdot(r-r_g)-\omega t]} d\omega}$$

where the final magnitude is determined by a free parameter $\boldsymbol{q}$. For the results displayed, $\boldsymbol{q}$ was chosen to give a comparable magnitude of the second wave packet (q=100). Methodologically, a justification for this multiplicative factor can be made by assuming that very little leakage occurs without the occurrence of atmospheric resonance, noting that the current lower atmospheric methodology cannot support the phenomena without resolving the vertical temperature profile (Godin et. al. 2020). Preliminary calculations suggest a magnitude increase when considering the thermal variation using the full MSIS profile, however a more in-depth treatment of atmospheric resonance is certainly needed rather than this simplified approach. Other contributing factors that have potential to increase the magnitude, and are not included in the current methodology, might include non-linear propagation affects, interaction with topography, or even the neutral dynamo as it is known the modes typically associated with atmospheric resonance have model energy densities near the E-region at ~80-120 km (Gille, J. C. 1966; Balachandran, N. K. 1968; Watada S.1995; Godin et. al. 2020).

Figures: